

# Inverted and Parallel Kerr Resonator System

## An exploratory project

Author :  
**Diego Polimeni**



Semester project done under the supervision of  
Postdoc. **Léo Paul Peyruchat**  
in the Hybrid Quantum Circuits Laboratory (HQC)  
led by prof. **Pasquale Scarlino**.

École polytechnique fédérale de Lausanne

Lausanne, EPFL, 2024



# Contents

|  |           |
|--|-----------|
| <b>Introduction</b>  | <b>1</b>  |
| <b>I Theory of Kerr Resonators</b>                               | <b>3</b>  |
| <b>1 Theory of Kerr Resonators</b>                               | <b>5</b>  |
| 1.1 Circuit Quantization . . . . .                               | 5         |
| 1.2 The Josephson Junction . . . . .                             | 7         |
| 1.3 Kerr Approximation - Transmon . . . . .                      | 9         |
| 1.4 Semi-classical response of a non-linear oscillator . . . . . | 9         |
| 1.4.1 Quantum limit . . . . .                                    | 12        |
| 1.5 Coupling multiple oscillators . . . . .                      | 13        |
| 1.5.1 Dimer . . . . .  | 14        |
| 1.5.2 Trimer . . . . .   | 15        |
| <b>II Inverted and Parallel<br/>Kerr Resonators</b>              | <b>17</b> |
| <b>2 Inverted and Parallel Kerr Resonators</b>                   | <b>19</b> |
| 2.1 Mode Localization . . . . .                                  | 19        |
| 2.2 Parallel Kerr . . . . .                                      | 22        |
| 2.2.1 $\omega_l = \omega_r$ . . . . .                            | 23        |
| 2.2.2 $\omega_l > \omega_r$ . . . . .                            | 25        |
| 2.3 Inverted Kerr . . . . .                                      | 28        |
| 2.3.1 $\omega_l = \omega_r$ . . . . .                            | 28        |
| 2.3.2 $\omega_l < \omega_r$ . . . . .                            | 31        |
| <b>III Tunable non-linearity devices</b>                         | <b>35</b> |
| <b>3 Tunable non-linearity devices</b>                           | <b>37</b> |
| 3.1 SQUID . . . . .  | 37        |
| 3.2 Array of SQUIDs . . . . .                                    | 38        |
| 3.3 RF-SQUID . . . . .   | 40        |

**Contents**

---

|           |                               |           |
|-----------|-------------------------------|-----------|
| 3.3.1     | Numeric simulations . . . . . | 42        |
| 3.4       | Array of RF-SQUIDS . . . . .  | 44        |
| 3.4.1     | Equivalent circuit . . . . .  | 44        |
| <b>IV</b> | <b>Experimental Design</b>    | <b>47</b> |
|           | <b>Bibliography</b>           | <b>50</b> |

# Introduction

This document contains the theory and results of a semester-long project done under the supervision of postdoc. Léo Paul Peyruchat in the Hybrid Quantum Circuits Laboratory (HQC) led by prof. Pasquale Scarlino at EPFL.

The project is exploratory in nature as we wanted to investigate the interaction of Kerr resonators, when the Kerr non-linearity was tuned for taking positive or negative values, in a semi-classical picture.

The outline of the document is the following: in the first part we develop the theory of Kerr Resonators starting with a brief summary of the basics of superconducting circuit technology and a mention to the transmon limit. Then, the analytical semi-classical response of a non linear oscillator is derived, . At the end of the chapter, we explore the theory of how to couple multiple oscillator, with particular attention to the case of two (dimer) and three (trimer) oscillators.

In the second chapter, we explore what we call an inverted/parallel Kerr resonator system, discussing mode localization for both cases. Numerical simulations of the semi-classical system are run and results analyzed and discussed.

In the third chapter, we focus our attention on the experimental realization of the systems investigated in the previous chapter. We briefly summarize the well-known results on the quantity of interest for a SQUID and an array of SQUIDs. Then, we examine analytically and numerically an RF-SQUID and an array of RF-SQUIDs.

The fourth chapter is devoted to the experimental design of the system.



# **Theory of Kerr Resonators**

## **Part I**





# 1 Theory of Kerr Resonators

## 1.1 Circuit Quantization

Transitioning from the classical to the quantum depiction of electrical circuits seamlessly occurs within the framework of the Hamiltonian description of the system. Exploiting the correspondence principle, classical variables are substituted with equivalent operators, and the Hamiltonian function is transformed into a function involving these operators, in the following fashion:

$$\begin{aligned}\phi &\rightarrow \hat{\phi} \\ q &\rightarrow \hat{q} \\ \mathcal{H} &\rightarrow \hat{\mathcal{H}}\end{aligned}$$

If the electric state of node  $n$  of a circuit, described by  $\phi_n$  and  $q_n$ , is a true degree of freedom of the circuit, meaning that neither  $\phi_n$ ,  $q_n$  or their derivatives are constants of motion, the two variables are conjugate variables, that don't commute with each other. In fact:

$$[\hat{\phi}_n, \hat{q}_n] = i\hbar \quad (1.1)$$

Exploiting this prescription the LC oscillator can be quantized; since the circuit as only one active node, one variable of flux and one variable of charge are sufficient for its description. The well-known Hamiltonian for a classical LC circuit is transferred to a quantum framework:

$$\mathcal{H} = \frac{q^2}{2C} + \frac{\phi^2}{2L} \quad (1.2)$$

The Hamiltonian can be written in second-quantized form using the following definitions:

$$\begin{aligned}\phi &= \phi_{\text{ZPF}} (c + c^\dagger) \\ q &= \frac{1}{i} q_{\text{ZPF}} (c - c^\dagger)\end{aligned} \quad (1.3)$$

## Chapter 1. Theory of Kerr Resonators

---

where  $c$  and  $c^\dagger$  are the annihilation and creation operators, respectively, which satisfy the commutation relation:

$$[c, c^\dagger] = 1 \quad (1.4)$$

The (normal-ordered) Hamiltonian operator writes:

$$\mathcal{H} = \frac{\hbar\omega_0}{2} (c^\dagger c + c c^\dagger) = \hbar\omega_0 \left( c^\dagger c + \frac{1}{2} \right) \quad (1.5)$$

where one defines the resonant frequency  $\omega_0$ , the impedance on resonance  $Z_0$  as:

$$\begin{aligned} \omega_0 &= \sqrt{\frac{1}{LC}} \\ Z_0 &= \sqrt{\frac{L}{C}} \end{aligned} \quad (1.6)$$

and the zero-point fluctuations i.e. the standard deviations of fluctuations from the ground state, in flux and in charge as:

$$\begin{aligned} \phi_{\text{ZPF}} &= \sqrt{\frac{\hbar Z_0}{2}} \\ q_{\text{ZPF}} &= \sqrt{\frac{\hbar}{2Z_0}} \end{aligned} \quad (1.7)$$

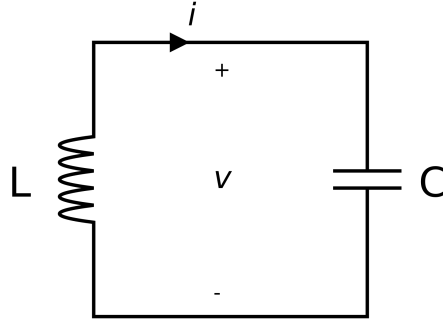


Figure 1.1: LC circuit diagram

The Hamiltonian in Eq. (1.5) is the quantum harmonic oscillator Hamiltonian. The eigenenergies associated with this Hamiltonian are:

$$E_n = \hbar\omega_0 \left( c^\dagger c + \frac{1}{2} \right) \quad (1.8)$$

Defining the anharmonicity of the Hamiltonian as the difference in frequency between two consecutive transition, i.e.:

$$\eta = \frac{\Delta E_1 - \Delta E_0}{\hbar} \quad \Delta E_n = E_{n+1} - E_n \quad (1.9)$$

one can easily appreciate that the such quantity is zero for an harmonic oscillator, meaning that its energy ladder is equally spaced.

Finally, it could be convenient, in some cases, to use a slightly different prescription for circuit quantization, that relies on the impedance:

$$\zeta = \sqrt{\frac{4E_C}{E_L + E_J/2}} \quad (1.10)$$

Such that the creation and annihilation operators, satisfying Eq. 1.1, are defined as:

$$\begin{aligned} \hat{b} &= \frac{1}{\sqrt{2}} \left( \frac{1}{\sqrt{\zeta}} \hat{\phi} - i\sqrt{\zeta} \hat{n} \right), \\ \hat{b}^\dagger &= \frac{1}{\sqrt{2}} \left( \frac{1}{\sqrt{\zeta}} \hat{\phi} + i\sqrt{\zeta} \hat{n} \right), \end{aligned} \quad (1.11)$$

Expressing the flux and conjugate momentum operators in terms of the annihilation and creation operators, one obtains:

$$\begin{aligned} \hat{\phi} &= \sqrt{\frac{\zeta}{2}} (\hat{b} + \hat{b}^\dagger) \\ \hat{n} &= \frac{i}{\sqrt{2\zeta}} (\hat{b} - \hat{b}^\dagger) \end{aligned} \quad (1.12)$$

It is possible to switch from the dimensionless prescription (Eq. 1.12) to the usual one (Eq. 1.3) by multiplying the impedance in Eq.1.10 by a factor of  $\frac{1}{2\pi} \frac{h}{2e^2}$ , which involves the resistance quantum  $R_Q = h/(2e)^2 \simeq 6.45\text{k}\Omega$ .

## 1.2 The Josephson Junction

In order to define a computational basis in a quantum computing context one needs to establish an effective two-level system. The quantum harmonic oscillator is not a wise choice, since its zero anharmonicity would lead to the excitation of higher energy level when probing the state of the system, which would lead to information leakage. In order to realize the widely used charge qubit, deriving from the quantum harmonic oscillator, the linear inductor is replaced by a dispersionless non-linear component called Josephson Junction. A Josephson junction is a device consisting of two superconductors separated by a thin insulating barrier or a weak link. According to the BCS theory, electrons within a superconductor combine into Cooper pairs, collectively behaving as bosons and described by a macroscopic collective wavefunction. This enables the superconductor to be characterized by a macroscopic phase and a local density of Cooper pairs. In 1962, Brian Josephson proposed that, when the insulating layer separating two electrodes is sufficiently thin, their wavefunctions overlap. This overlap facilitates the tunneling of Cooper pairs through the insulating layer, resulting in a dissipation-free supercurrent, an effect known as the Josephson effect. The behavior is

## Chapter 1. Theory of Kerr Resonators

---

mathematically described by the first and second Josephson relations:

$$I_J(t) = I_0 \sin \delta(t) \quad (1.13)$$

$$V = \frac{\Phi_0}{2\pi} \dot{\delta} \quad (1.14)$$

where  $I_0$  is the critical current of the junction,  $\delta$  the gauge-invariant phase difference across the junction,  $V$  the voltage across the junction and  $\Phi_0 = \frac{h}{2e}$  the superconducting flux quantum. The dynamical behavior of these two equations can be understood by first differentiating Eq. (1.13) and replacing  $\dot{\delta}$  with  $V$  according to Eq. (1.14):

$$\frac{dI_J}{dt} = I_0 \cos \delta \frac{2\pi}{\Phi_0} V \quad (1.15)$$

With  $dI_J/dt$  proportional to  $V$ , this equation describes an inductor. By defining a Josephson inductance  $L_J$  according to the conventional definition  $V = L_J dI_J/dt$ , one finds

$$L_J = \frac{\Phi_0}{2\pi I_0 \cos \delta} \quad (1.16)$$

The  $1/\cos \delta$  term reveals that this inductance is nonlinear. It becomes large as  $\delta \rightarrow \pi/2$ , and is negative for  $\pi/2 < \delta < 3\pi/2$ . The inductance at zero bias is  $L_{J0} = \Phi_0/2\pi I_0$ .

An inductance describes an energy-conserving circuit element. The energy stored in the junction is given by

$$\begin{aligned} U_J &= \int I_J V dt = \int I_0 \sin \delta \frac{\Phi_0}{2\pi} \frac{d\delta}{dt} dt \\ &= \frac{I_0 \Phi_0}{2\pi} \int \sin \delta d\delta = -\frac{I_0 \Phi_0}{2\pi} \cos \delta. \end{aligned} \quad (1.17)$$

where the term  $E_J = \frac{I_0 \Phi_0}{2\pi}$  is the intrinsic Josephson energy of the junction. This calculation of energy can be generalized for other non-dissipative circuit elements. On the contrary, if a circuit element has an energy  $U(\delta)$ , then the current-phase relationship of the element, analogously to Eq. (1.13), is

$$I_J(\delta) = \frac{2\pi}{\Phi_0} \frac{\partial U(\delta)}{\partial \delta} \quad (1.18)$$

A generalized Josephson inductance can also be found from the second derivative of  $U$ ,

$$\frac{1}{L_J} = \left( \frac{2\pi}{\Phi_0} \right)^2 \frac{\partial^2 U(\delta)}{\partial \delta^2} \quad (1.19)$$

### 1.3 Kerr Approximation - Transmon

In order to illustrate the Kerr approximation for a non-linear device involving a Josephson Junction, we analyse the well-known transmon limit of a superconducting charge qubit. The name 'Transmon qubit' is an abbreviation of the term transmission line shunted plasma oscillation qubit. It is closely related to a Cooper-pair box, while operating in a regime where  $E_J/E_C \gg 1$ . The Hamiltonian of a transmon qubit is:

$$H = 4E_C \hat{n}^2 - E_J \cos \hat{\phi}, \quad (1.20)$$

where  $\hat{n} = -i \left( \frac{E_J}{8E_C} \right)^{1/4} \frac{1}{\sqrt{2}} (\hat{a} - \hat{a}^\dagger)$  and  $\hat{\phi} = \left( \frac{2E_C}{E_J} \right)^{1/4} (\hat{a} + \hat{a}^\dagger)$  is the conjugate pair of position and momentum,  $E_C = \frac{e^2}{2C_\Sigma}$  is the Coulomb charging energy corresponding to one electron on the total junction capacitance  $C_\Sigma$ , and  $E_J$  is the Josephson energy. Since  $E_J/E_C \gg 1$ , and therefore  $\Delta\hat{\phi} \ll 1$ , one can Taylor-expand the cosine term truncate it to its first nonlinear correction leading to the approximate transmon Hamiltonian:

$$\hat{H}_q = 4E_C \hat{n}^2 + \frac{1}{2} E_J \hat{\phi}^2 - \frac{1}{4!} E_J \hat{\phi}^4 \quad (1.21)$$

As expected from the previous discussion, the transmon is thus a weakly anharmonic oscillator. Note that the  $2\pi$  periodicity of the Hamiltonian is broken under this approximation. Using the second-quantized definition of the flux and charge operators, one finds the Kerr Hamiltonian:

$$\begin{aligned} \hat{H}_q &= \sqrt{8E_C E_J} \hat{a}^\dagger \hat{a} - \frac{E_C}{12} (\hat{a}^\dagger + \hat{a})^4 \\ &\approx \hbar\omega_q \hat{a}^\dagger \hat{a} - \frac{E_C}{2} \hat{a}^\dagger \hat{a}^\dagger \hat{a} \hat{a} \end{aligned} \quad (1.22)$$

where  $\hbar\omega_q = \sqrt{8E_C E_J} - E_C$ . On the second line, we have kept only the terms that have the same number of creation and annihilation operators. This is reasonable because, in a frame rotating at  $\omega_q$ , any terms with an unequal number of  $\hat{a}$  and  $\hat{a}^\dagger$  will oscillate. If the frequency of these oscillations is larger than the prefactor of the oscillating term, then this term rapidly averages out and can be neglected.

### 1.4 Semi-classical response of a non-linear oscillator

In this section we describe the behavior of a weakly non-linear system interacting with the environment. We can describe such a system by considering the Hamiltonian of a harmonic oscillator with a Kerr non-linearity  $K$ , where  $K < 0$ :

$$\mathcal{H} = \hbar\omega_0 \hat{a}^\dagger \hat{a} + \frac{\hbar K}{2} \hat{a}^\dagger \hat{a}^\dagger \hat{a} \hat{a} \quad (1.23)$$

If the system possesses an external coupling and internal losses, these factors can be considered by applying input-output theory. When a strong coherent field  $\alpha$  is applied to the system, the interaction can be described using semiclassical modeling. The nonlinear resonator is

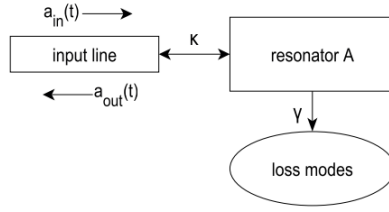


Figure 1.2: Input-Output schema for a single resonator

coupled with rate  $\kappa$  to a transmission line, through which the pump and signal fields propagate. On the basis of this model and the Hamiltonian in Eq. (1.23) we obtain the following equation of motion for the intracavity field:

$$\dot{A} = -i\tilde{\omega}_0 A - iKA^\dagger AA - \frac{\kappa + \gamma}{2} A + \sqrt{\kappa} A_{\text{in}}(t) + \sqrt{\gamma} b_{\text{in}}(t) \quad (1.24)$$

In addition to coupling to the transmission line modes  $A_{\text{in}}(t)$  with rate  $\kappa$  we account for potential radiation loss mechanisms by introducing the coupling to modes  $b_{\text{in}}(t)$  with loss rate  $\gamma$ . A boundary condition equivalent to

$$A_{\text{out}}(t) = \sqrt{\kappa} A(t) - A_{\text{in}}(t) \quad (1.25)$$

also holds for the loss modes. We define the drive strength  $F = \sqrt{\kappa} A_{\text{in}}$  and the drive power  $P = \hbar\omega_0 |A_{\text{in}}|^2$  and the relation between the two is given by  $F = \sqrt{\frac{\kappa P}{\hbar\omega_0}}$ . The input field  $A_{\text{in}}$  is typically a sum of a strong coherent pump field and an additional weak signal field. Since this signal carries at least vacuum noise, it is treated as a quantum field. In this formalism, this particular situation is accounted for by decomposing each field mode into a sum of a classical part and a quantum part.

$$\begin{aligned} A_{\text{in}}(t) &= (a_{\text{in}}(t) + \alpha_{\text{in}}) e^{-i\omega_p t}, \\ A_{\text{out}}(t) &= (a_{\text{out}}(t) + \alpha_{\text{out}}) e^{-i\omega_p t}, \\ A(t) &= (a(t) + \alpha) e^{-i\omega_p t}, \end{aligned} \quad (1.26)$$

where  $\alpha, \alpha_{\text{in}}, \alpha_{\text{out}}$  represent the classical parts of the field which are associated with the pump,

## 1.4 Semi-classical response of a non-linear oscillator

while  $a, a_{\text{in}}, a_{\text{out}}$  account for the quantum signal fields. Since all  $\alpha$ 's are complex numbers, the modes  $a$  satisfy the same bosonic commutation relations as modes  $A$  do. Multiplying the field modes by the additional exponential factor  $e^{-i\omega_p t}$ , one works in a frame rotating at the pump frequency  $\omega_p$ .

The steady state solution for the coherent pump field is determined by

$$iK\alpha|\alpha|^2 + \left(i(\omega_0 - \omega_p) + \frac{\kappa + \gamma}{2}\right)\alpha = \sqrt{\kappa}\alpha_{\text{in}} \quad (1.27)$$

which follows immediately by substituting Eq. (1.24) into Eq. (1.23). By multiplying both sides with their complex conjugate we get to the equation

$$\frac{\kappa}{(\kappa + \gamma)^2} |\alpha_{\text{in}}|^2 = \left( \left( \frac{\omega_p - \omega_0}{\kappa + \gamma} \right)^2 + \frac{1}{4} \right) |\alpha|^2 - \frac{2(\omega_p - \omega_0)K}{(\kappa + \gamma)^2} |\alpha|^4 + \left( \frac{K}{\kappa + \gamma} \right)^2 |\alpha|^6, \quad (1.28)$$

which determines the average number of pump photons  $n \propto |\alpha|^2$  in the resonator. It is convenient to introduce the following scale-invariant quantities:  $\delta$  is the detuning between pump and resonator frequency in units of the total resonator linewidth,  $\tilde{\alpha}_{\text{in}}$  is the dimensionless drive amplitude, and  $\xi$  is the product of drive power and nonlinearity, also expressed in dimensionless units. Finally,  $n$  is the mean number of pump photons in the resonator relative to the incident pump power.

$$\delta \equiv \frac{\omega_p - \omega_0}{\kappa + \gamma}, \quad \tilde{\alpha}_{\text{in}} \equiv \frac{\sqrt{\kappa}\alpha_{\text{in}}}{\kappa + \gamma}, \quad \xi \equiv \frac{|\tilde{\alpha}_{\text{in}}|^2 K}{\kappa + \gamma}, \quad n \equiv \frac{|\alpha|^2}{|\tilde{\alpha}_{\text{in}}|^2} \quad (1.29)$$

Using such definition, Eq.(1.28) can be reduced to a cubic equation in the mean number of photons  $n$  in the resonator:

$$1 = \left( \delta^2 + \frac{1}{4} \right) n - 2\delta\xi n^2 + \xi^2 n^3 \quad (1.30)$$

A significant implication of this is that, according to Eq. (1.29), the dynamics is determined by the product of drive power and non-linearity, rather than by each quantity individually. Consequently, it is possible, in theory, to offset the effects of a small nonlinearity by increasing the drive power. This means that properties like the gain-bandwidth product remain unaffected by the strength of the nonlinearity, as long as the pump power is significantly greater than the power of amplified fluctuations.

In Fig.1.3a it is plotted the mean photon number in the cavity  $n$  for various parameters  $\xi$  as a function of the detuning  $\delta$ . At the critical value  $\xi_{\text{crit}} = -1/\sqrt{27}$  the derivative  $\partial n/\partial \delta$  diverges and thus the response of the parametric amplifier becomes extremely sensitive to small changes. For even stronger effective drive powers  $\xi/\xi_{\text{crit}} > 1$  the cubic Eq. (1.30) has three real solutions. The solutions for the high and low photon numbers are stable, while the intermediate one is unstable. The system bifurcates in this regime and becomes bistable.

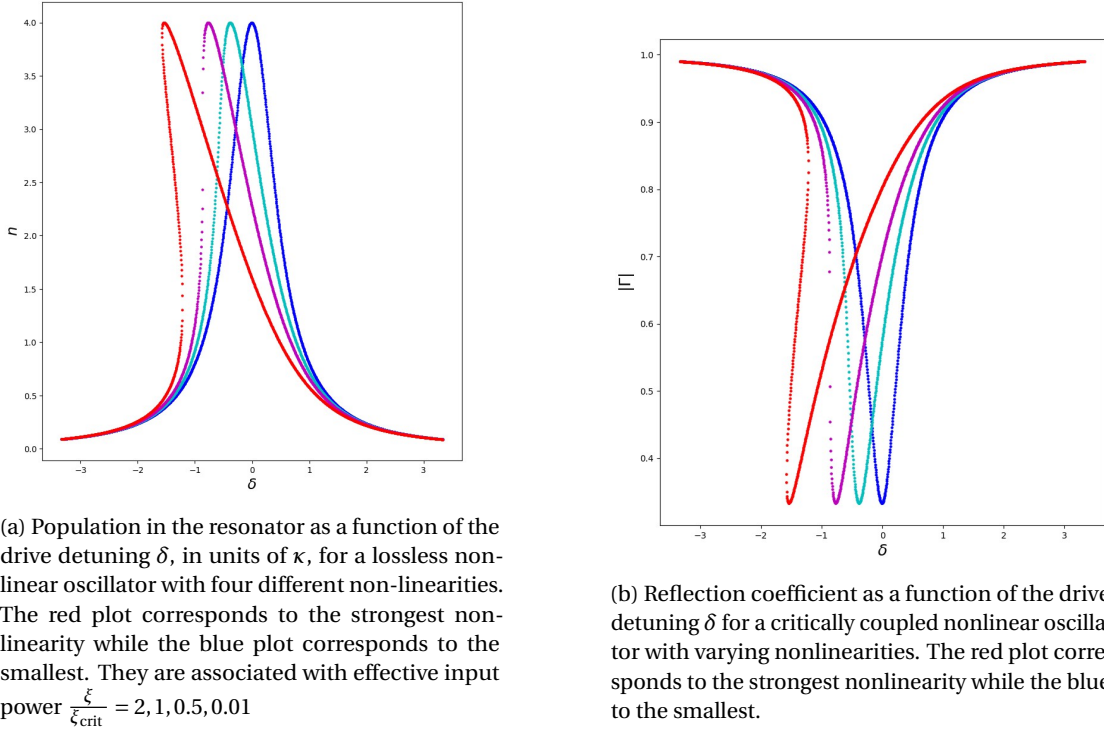


Figure 1.3: Characterisation of the bistable regime of a semiclassical non linear oscillator

Always in the case where  $\xi/\xi_{\text{crit}} > 1$ , The critical detuning below which the system enters the bistable region is  $\delta_{\text{crit}} = -\sqrt{3}/2$ . The critical point  $(\xi_{\text{crit}}, \delta_{\text{crit}})$  is the one at which both  $\partial\delta/\partial n$  and  $\partial^2\delta/\partial^2 n$  vanish.

Experimentally, the system parameters are characterized by measuring the complex reflection coefficient  $\Gamma \equiv \alpha_{\text{out}}/\alpha_{\text{in}}$ .

$$\Gamma = \frac{\kappa}{\kappa + \gamma} \frac{1}{\frac{1}{2} - i\delta + i\xi n} - 1 \quad (1.31)$$

In Fig.1.3b it is plotted the absolute value of the reflection coefficient at  $\xi = \xi_{\text{crit}}$  for various nonlinearities.

### 1.4.1 Quantum limit

Up until now we considered a strong coherent field  $\alpha$  as being applied to the system. This implies, as mentioned, that the average number of photons in the cavity is high and the system can be treated semi-classically as shown in the previous section. For a low photon number, however, a semi-classical description fails in describing the properties of the system. In this case, one should use a full-quantum description of the system and environment. This is achieved, in the context of Open Quantum Systems, by using the Lindblad Master Equation. For a system with the Hamiltonian of Eq. (1.23), and the dynamics of the density matrix  $\rho$



describing the state of the system follows:

$$\frac{\partial \hat{\rho}}{\partial t} = -i[\hat{H}, \hat{\rho}] + \Gamma^{(k)} \left( \hat{L}^{(k)} \hat{\rho} \hat{L}^{(k)\dagger} - \frac{1}{2} \{ \hat{L}^{(k)\dagger} \hat{L}^{(k)}, \hat{\rho} \} \right) \quad (1.32)$$

where  $\Gamma^{(k)}$  can be the dissipation or the dephasing rate. Then one should solve Eq. (1.32) for the steady state, that is,  $\frac{d\rho}{dt} = 0$ . Since for an Open Quantum System, at least one steady state exists and the system will relax to it, many algorithms exist to retrieve it. We mention the ordinary method, mesolve, the Monte - Carlo wavefunction method, the Arnoldi Lindblad algorithm, and the sets of variational Quantum Algorithms. CITE

## 1.5 Coupling multiple oscillators

In this section, we will obtain the Hamiltonian for a system consisting of multiple resonators that are capacitively coupled. To begin, let us consider the Lagrangian of an electric circuit with  $N$  LC parallel oscillators that are capacitively coupled to each other. The coordinate for each oscillator is taken as the mode flux, denoted by  $V_i = \dot{\phi}_i$ . The Lagrangian can be expressed as:

$$\mathcal{L} = \sum_{i=1}^N \frac{1}{2} C_i \dot{\phi}_i^2 + \sum_{i=1}^N \frac{1}{2} C_{ji} (\dot{\phi}_i - \dot{\phi}_{i+1})^2 - \sum_{i=1}^N \frac{1}{2L_i} \phi_i^2 \quad (1.33)$$

where the first contribution corresponds to the shunt capacitors, the second to the coupling capacitors, and the third to the shunt inductances. Ther Lagrangian can be written in matrix form as:

$$\mathcal{L} = \frac{1}{2} \dot{\Phi}^T C \dot{\Phi} - \frac{1}{2} \Phi^T L^{-1} \Phi \quad (1.34)$$

where  $\Phi = (\phi_1, \phi_2, \phi_3, \dots)$  is the flux vector,  $C$  the tridiagonal capacitance matrix ( $C_{ii} = C_i, C_{ii+1} = C_{i+1i} = C_{ji}$ ) and  $L^{-1}$  the inverse of the diagonal inductance matrix ( $L_{ii}^{-1} = 1/L_i$ ). Using the standard Lagrangian derivation, the charge operator is defined as:

$$q_i = \frac{\partial \mathcal{L}}{\partial \dot{\phi}_i} = C_{ij} \dot{\phi}_j \quad (1.35)$$

which allows us to write the Hamiltonian as

$$\mathcal{H} = \frac{1}{2} Q^T C^{-1} Q + \frac{1}{2} \Phi^T L^{-1} \Phi \quad (1.36)$$

where  $Q = (q_1, q_2, \dots)$  is the charge vector. We proceed now to upgrade the two canonical

## Chapter 1. Theory of Kerr Resonators

---

conjugate variables to operators described by the canonical commutation relation

$$[\hat{q}_i, \hat{\phi}_j] = -i\hbar\delta_{ij} \quad (1.37)$$

Now we can define second-quantization operators to reach the expression:

$$\mathcal{H} = \sum_{i=1}^N \hbar\omega_i \left( \hat{a}_i^\dagger \hat{a}_i + \frac{1}{2} \right) + \sum_{j>i} \hbar J_{ij} \left( \hat{a}_i^\dagger \hat{a}_j + \hat{a}_j^\dagger \hat{a}_i \right) \quad (1.38)$$

where

$$\begin{aligned} \omega_i &= \sqrt{C_{ii}^{-1} L_{ii}^{-1}} \\ J_{ij} &= \frac{1}{2} \frac{C_{ij}^{-1}}{\sqrt{C_{ii}^{-1} C_{jj}^{-1}}} \sqrt{\omega_i \omega_j}. \end{aligned} \quad (1.39)$$

The Hamiltonian that describes nonlinear coupled resonators can be obtained introducing the Kerr term for each one of the resonators as following:

$$\mathcal{H} = \sum_{i=1}^N \hbar\omega_i \left( \hat{a}_i^\dagger \hat{a}_i + \frac{1}{2} \right) + \sum_{j>i} \hbar J_{ij} \left( \hat{a}_i^\dagger \hat{a}_j + \hat{a}_j^\dagger \hat{a}_i \right) + \sum_{i=1}^N \frac{K}{2} \hat{a}_i^\dagger \hat{a}_i^\dagger \hat{a}_i \hat{a}_i. \quad (1.40)$$

If we consider all resonator-resonator coupling interactions to be equal and only affecting nearest-neighbours, the Hamiltonian can be rewritten as

$$\mathcal{H} = -J \sum_{\langle i,j \rangle} \hat{a}_i^\dagger \hat{a}_j + \sum_i \epsilon_i \hat{n}_i + \frac{U}{2} \sum_i \hat{n}_i (\hat{n}_i - 1) \quad (1.41)$$

where  $\epsilon_i = \hbar\omega_i$ ,  $J = -\hbar J_{i,i+1}$ ,  $U = \hbar K$  and  $\hat{n}_i = \hat{a}_i^\dagger \hat{a}_i$  is the photon number operator. This is exactly the Hamiltonian of the Bose-Hubbard model, which approximately describes the interaction of bosons in a lattice.

### 1.5.1 Dimer

A device composed of two coupled driven-dissipative Kerr oscillators is called a Josephson parametric dimer. The Hamiltonian of the system can be written as:

$$\mathcal{H} = \sum_{i=1}^2 \hbar\omega_0 \left( \hat{a}_i^\dagger \hat{a}_i + \frac{1}{2} \right) + \sum_{i=1}^2 \frac{K}{2} \hat{a}_i^\dagger \hat{a}_i^\dagger \hat{a}_i \hat{a}_i + \hbar J \left( \hat{a}_1^\dagger \hat{a}_2 + \hat{a}_2^\dagger \hat{a}_1 \right) \quad (1.42)$$

where  $\omega_0$  is the resonant frequency of the resonators,  $K$  is the Kerr non-linearity,  $J$  is the coupling strength between the resonators. The one-photon loss processes are modelled via the Lindblad jump operators  $\hat{L}_j^{(1)} = \sqrt{\gamma_j} \hat{a}_j$ ,  $j = 1, 2$  and while the dephasing process via  $\hat{L}_j^{(2)} = \sqrt{\kappa_j} \hat{a}_j^\dagger \hat{a}_j$ ,  $j = 1, 2$ . If we diagonalize the Hamiltonian by ignoring the nonlinear term, we find the two hybridized modes and associated resonant frequencies:

$$a_{\pm} = \frac{a_1 \pm a_2}{\sqrt{2}} \quad \omega_{\pm} = \omega_0 \pm J \quad (1.43)$$

The hybridized modes coming out of the diagonalization procedure correspond to a sym-

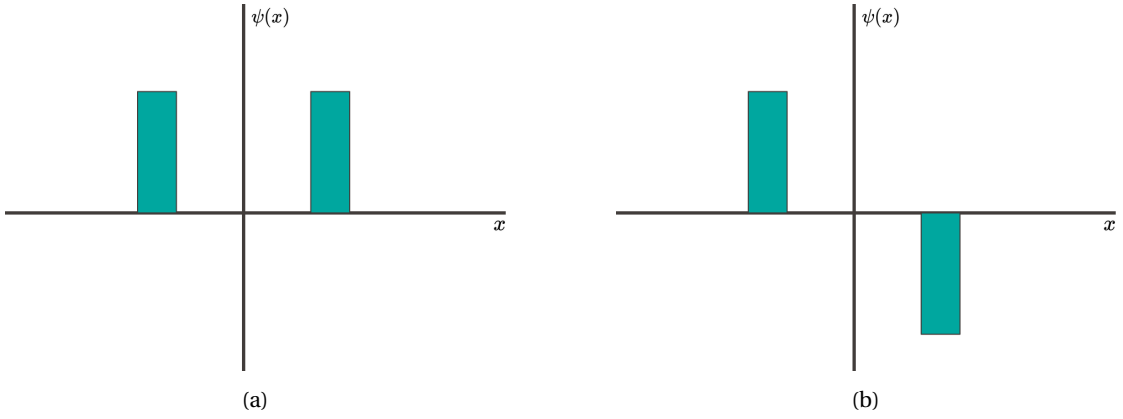


Figure 1.4: Symmetric (a) and antisymmetric (b) mode of a dimer.

metric and antisymmetric wavefunction, schematically represented on Fig. 1.4. The mode localization and coupling will largely depend on the initial detuning of the cavities and on the input power. This means that one could control mode localization fine-tuning the input power of the drive. To better understand the Kerr shift in a dimer, this phenomenon will be analysed more deeply in a following section.

### 1.5.2 Trimer

A device composed of three coupled nonlinear resonators is called a Josephson parametric trimer. Even though we have designed coupled systems with a higher number of resonators, the JPT is the natural continuation of the JPD and it is also the smallest system which can show next-nearest neighbour interactions.

The Hamiltonian of the system can be written as

$$\mathcal{H} = \sum_{i=1}^3 \hbar \omega_0 \left( \hat{a}_i^\dagger \hat{a}_i + \frac{1}{2} \right) + \sum_{j>i} \hbar J_{ij} \left( \hat{a}_i^\dagger \hat{a}_j + \hat{a}_j^\dagger \hat{a}_i \right) + \sum_{i=1}^3 \frac{K}{2} \hat{a}_i^\dagger \hat{a}_i^\dagger \hat{a}_i \hat{a}_i \quad (1.44)$$

where we consider the coupling between next-nearest neighbours, even though it is much

## Chapter 1. Theory of Kerr Resonators

---

smaller than the nearest-neighbour. We also consider that the resonance frequencies of the three resonators are the same. If we diagonalize the Hamiltonian by ignoring the nonlinear term and considering  $J_{13} \approx 0$ , we find three hybridized modes which can be written as

$$\begin{aligned} a_+ &= \frac{(a_R + a_L) + \sqrt{2}a_C}{2}, \\ a_0 &= \frac{a_R - a_L}{\sqrt{2}}, \\ a_- &= \frac{(a_R + a_L) - \sqrt{2}a_C}{2}, \end{aligned} \tag{1.45}$$

and with eigenfrequencies  $\omega_+ = \omega_0 + \sqrt{2}J$ ,  $\omega_C = \omega_0$ ,  $\omega_- = \omega_0 - \sqrt{2}J$ , where  $\omega_0$  is the bare resonance frequency of the resonators. The nonlinear term will shift the three eigenfrequencies proportionally to the applied coherent drive. If we solve the system by considering a strong classical field, as done in the previous section, we can plot the number of photons present in each of the resonators as a function of the detuning from the bare frequency.

# **Inverted and Parallel Part II**

## **Kerr Resonators**



## 2 Inverted and Parallel Kerr Resonators

In this section we focus our attention on the Josephson parametric dimer described in the previous section. We analyse the behaviour of the system when the resonators have same or opposite Kerr non-linearity. For each case, the different configuration of resonant frequencies are explored. Notice that a positive Kerr non-linearity will lead to a right shift of the resonant frequency as the input power increases while a negative Kerr non-linearity to left shift of the resonant frequency. We recall here that a system composed of two coupled resonator with resonant frequency  $\omega_0$  will have two eigenmodes with shifted eigenfrequencies  $\omega_{\pm} = \omega_0 \pm J$ . For terminology, we call parallel Kerr resonators two coupled resonators with the same Kerr non-linearity.

### 2.1 Mode Localization

As a preliminary step for the analysis of the Kerr shift phenomenon in a semiclassical context, it is capital to study the mode localization in the cavities of the dimer and how it is affected by the input power strength and position in space. To do so, in a similar way as in the previous section, we diagonalize the Hamiltonian of the dimer, taking into account internal couplings and losses. It has the following matrix form:

$$\frac{\mathcal{H}}{\hbar} = \begin{pmatrix} \omega_0 - \frac{\delta}{2} + i\frac{\kappa+\gamma}{2} & J \\ J & \omega_0 + \frac{\delta}{2} + i\frac{\kappa+\gamma}{2} \end{pmatrix} \quad (2.1)$$

where  $\omega_1 = \omega_0 - \frac{\delta}{2}$  is the resonant frequency of the first mode,  $\omega_2 = \omega_0 + \frac{\delta}{2}$  is the resonant frequency of the second mode,  $\delta$  is the detuning between the resonators,  $\kappa$  and  $\gamma$  are internal couplings and external losses, respectively. The hybridized ||normalize?|| modes and associated eigenfrequencies are:

$$\psi_{\pm} = \begin{pmatrix} \frac{\delta \pm \sqrt{\delta^2 + 4J^2}}{2J} \\ 1 \end{pmatrix} \quad \omega_{\pm} = \omega_0 + i\frac{\kappa+\gamma}{2} \pm \frac{1}{2}\sqrt{\delta^2 + 4J^2} \quad (2.2)$$

## Chapter 2. Inverted and Parallel Kerr Resonators

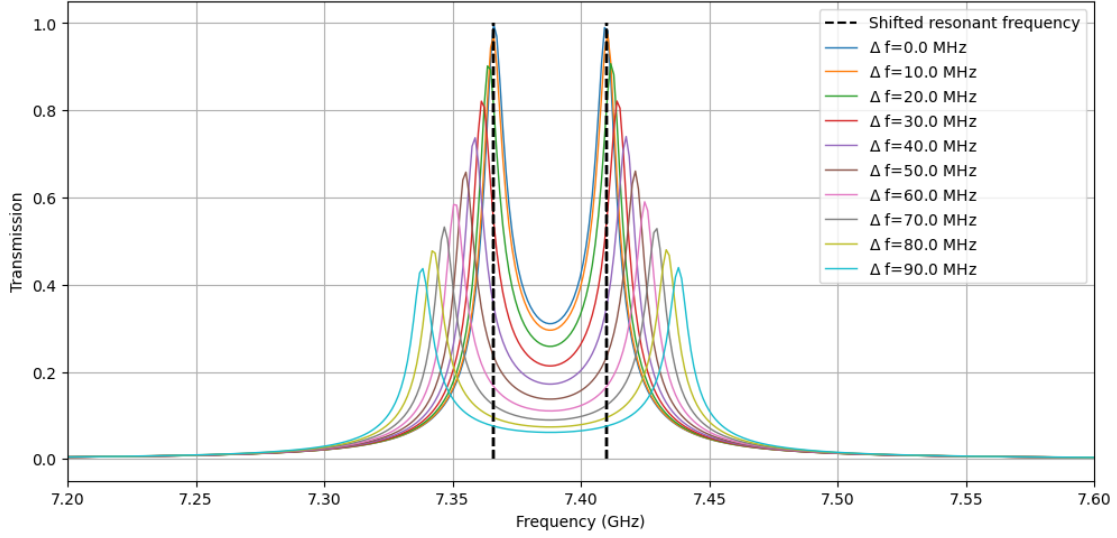


Figure 2.1: Transmission as a function of frequency for different detuning between the two resonator. The dashed lines correspond to a mode splitting of  $2J$ , for zero detuning between the cavities.

In this treatment, the mode splitting explicitly depends on the detuning  $\delta$  between the two resonators. On Fig. 2.1, the transmission spectrum of the dimer is plotted to account for this phenomenon. Notice that if we neglect internal couplings and external losses, the zero detuning case corresponds to the one described in Eq.(1.43) and it is depicted on Fig. 2.2. Fig. 2.2 specifically shows the mode splitting in frequency space for the uncoupled case, corresponding to dashed lines, and the coupled case, corresponding to solid lines. The asymptotic behaviour of the coupled modes approaches the one of the uncoupled modes, meaning that for large detuning the coupling can be neglected. On Fig. 2.3 and 2.4 is shown the probability density of the non-hybridized first and second mode, respectively. For zero detuning the modes are equally delocalized over the two cavities, while increasing the detuning progressively localize the first mode on left cavity and second mode on right cavity. It is of particular interest to notice that the combined effect of Kerr nonlinearity and input drive results in an effective detuning, as the mode splitting signature strictly resembles the one showed on Fig.2.2. This behaviour will appear from the numerical results of the following section. As



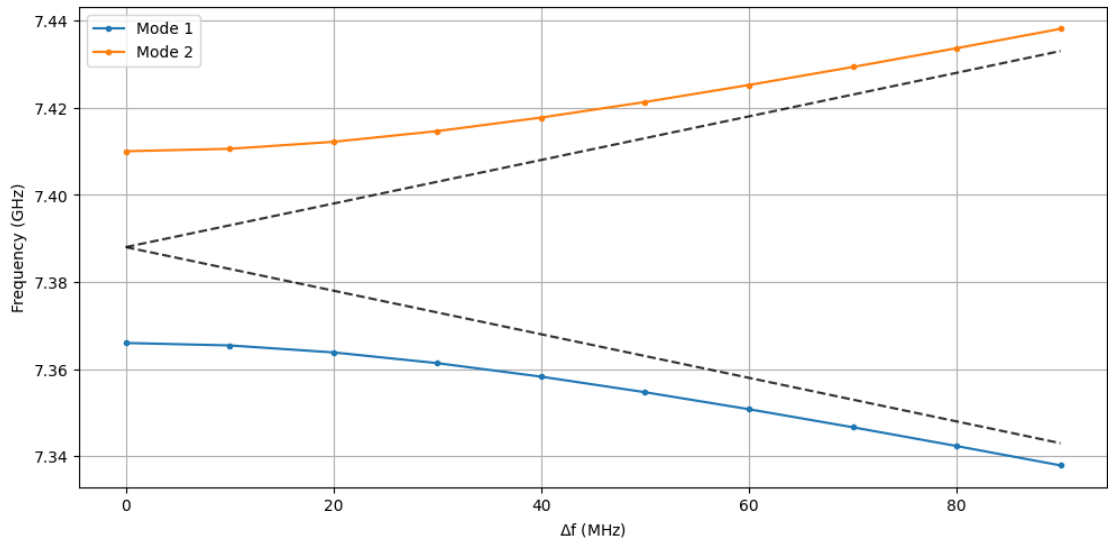


Figure 2.2: Resonant frequency of the two initial modes as a function of the the detuning between the two resonators

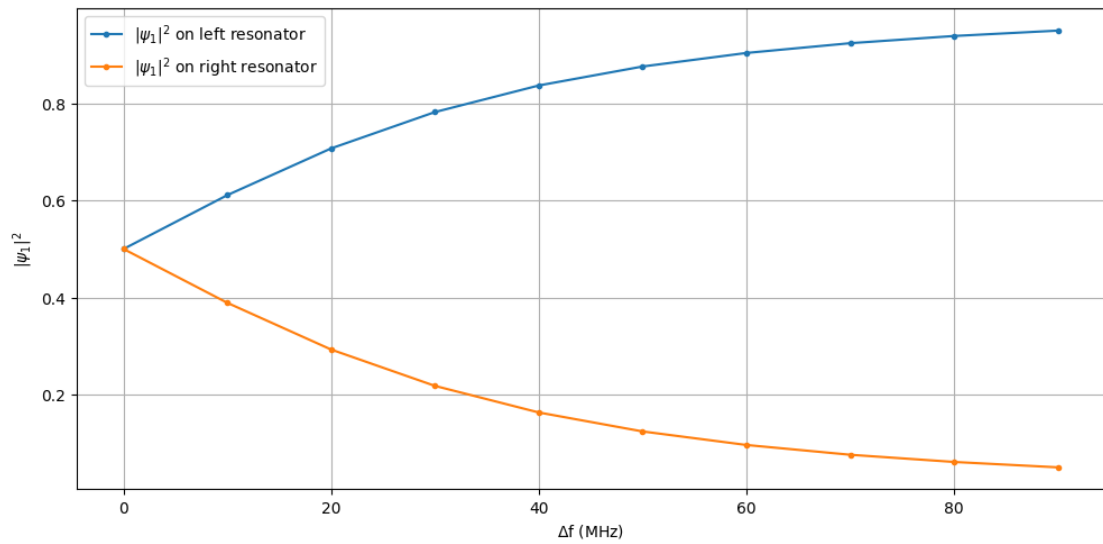


Figure 2.3: Spatial distribution of the first mode

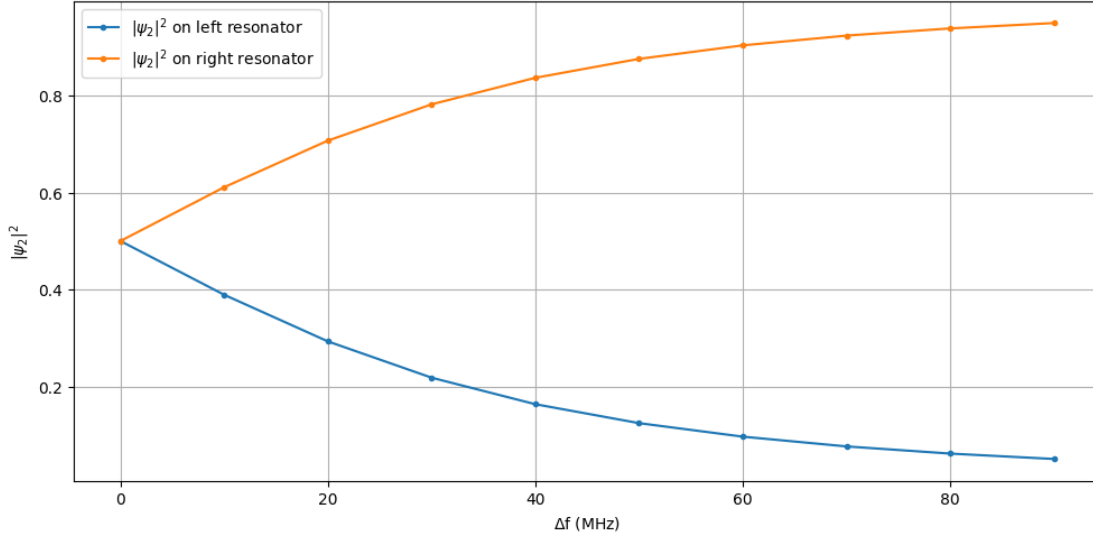


Figure 2.4: Spatial distribution of the second mode

## 2.2 Parallel Kerr

In this section we analyse the behaviour of parallel Kerr resonators; on Fig. 2.5 are represented the two configuration of interest, where dashed lines correspond to uncoupled modes and solid lines correspond to coupled modes. On Fig.2.5a the two resonator have the same resonant frequency; without coupling the two modes occupy the same position in frequency space and undergo a Kerr shift with the same slope, while with coupling they are set apart by  $2J$  and still undergo a Kerr shift with the same slope. On Fig.2.5b the two resonator have different resonant frequency; without coupling the two modes occupy different position in frequency space and undergo a Kerr shift with the same slope, while with coupling they are additionally set apart by  $2J$  and one of the modes has a much more apparent Kerr shift as an effect of the mode localization due to the effective detuning. The case of figure represented, corresponds to the one in which left drive is applied, effectively bending the left mode more. A right drive would have an analogous effect on the right mode. The simulation are performed with  $K_l = K_r = 0.1$  GHz. An intercavity coupling  $J = 100$  MHz is applied while internal coupling are set to  $\kappa = 10$  MHz and external losses are set to  $\gamma = 20$  MHz. The input drive strength is initially set at  $F = 0.5$  MHz and later varied in a range going from 0.1 MHz to 5 MHz. The equation of motion for the semi-classical fields are numerically integrated using the Runge-Kutta method of order 5.

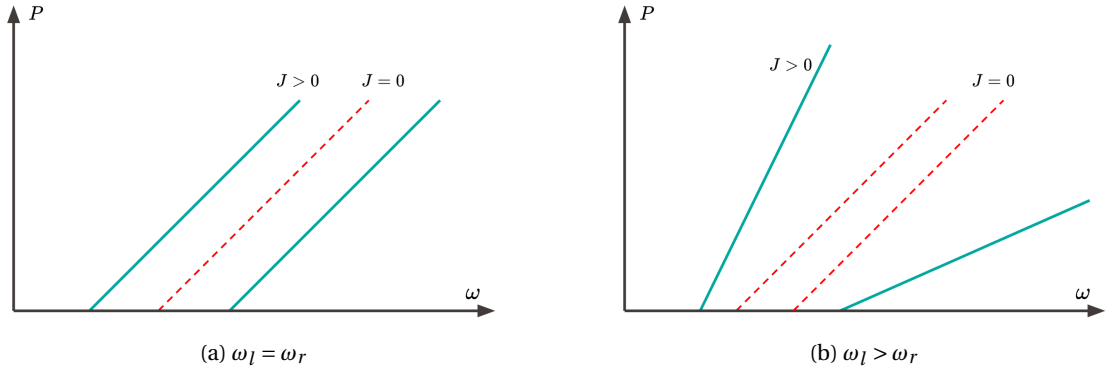


Figure 2.5: Schematic representation of the Kerr shift in a parallel Kerr dimer: dashed lines represent the uncoupled modes, solid lines represent the hybridized modes

### 2.2.1 $\omega_l = \omega_r$

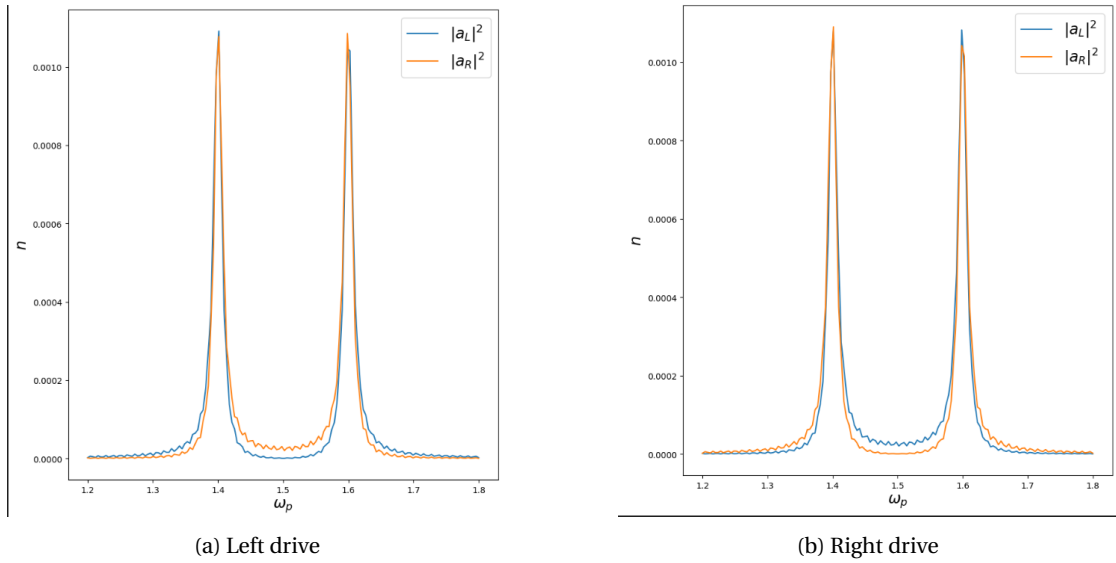


Figure 2.6: Modulus squared of the left and right cavity fields as a function of the pump frequency when the drive is applied on the left cavity (a) or on the right cavity (b) for  $K_l = K_r$  and  $\omega_l = \omega_r$

We start by analyzing the configuration in which  $\omega_l/2\pi = \omega_r/2\pi = 1.5$  GHz. Fig. 2.6 shows the modulus squared of the cavity fields when the pump frequency is varied between 1.2 GHz and 1.8 GHz. As expected two Lorentzian centered at the shifted resonant frequency of the coupled resonators appears. The two modes are completely delocalized over the two cavities and since the system is completely symmetric, applying the drive on the left or on the right is not relevant.

On Fig. 2.7 and 2.8 is shown the cavity fields landscape as a function of the pump frequency and input drive strength and one can appreciate the right Kerr shift of the cavity modes. As

## Chapter 2. Inverted and Parallel Kerr Resonators

explained previously for a single Kerr resonator, one can appreciate two bi-stable regions, one for each resonator, corresponding to phase transitions. It must be noted that only the bottom part of the plot has relevant physical meaning; in fact, in this region the semiclassical approximation is valid, while when the two lines start to overlap the full quantum simulation forecasts a merging region in which quantum chaos arises and could be examined.

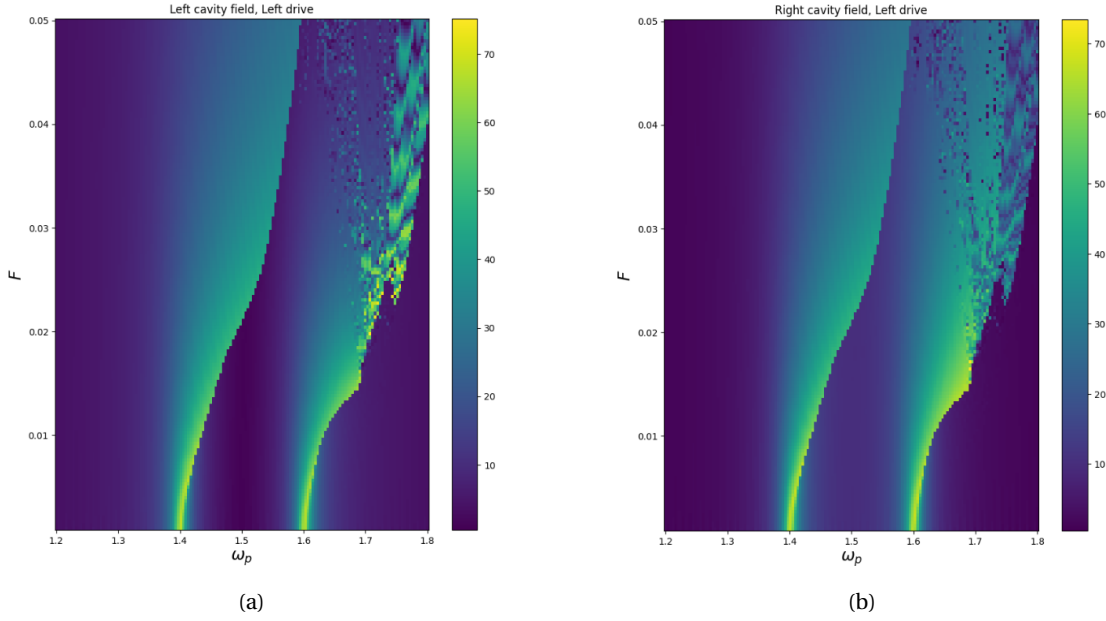


Figure 2.7: Modulus squared of the left (a) and right (b) cavity fields as a function of the pump frequency and the input power when the drive is applied on the left cavity for  $K_l = K_r$  and  $\omega_l = \omega_r$

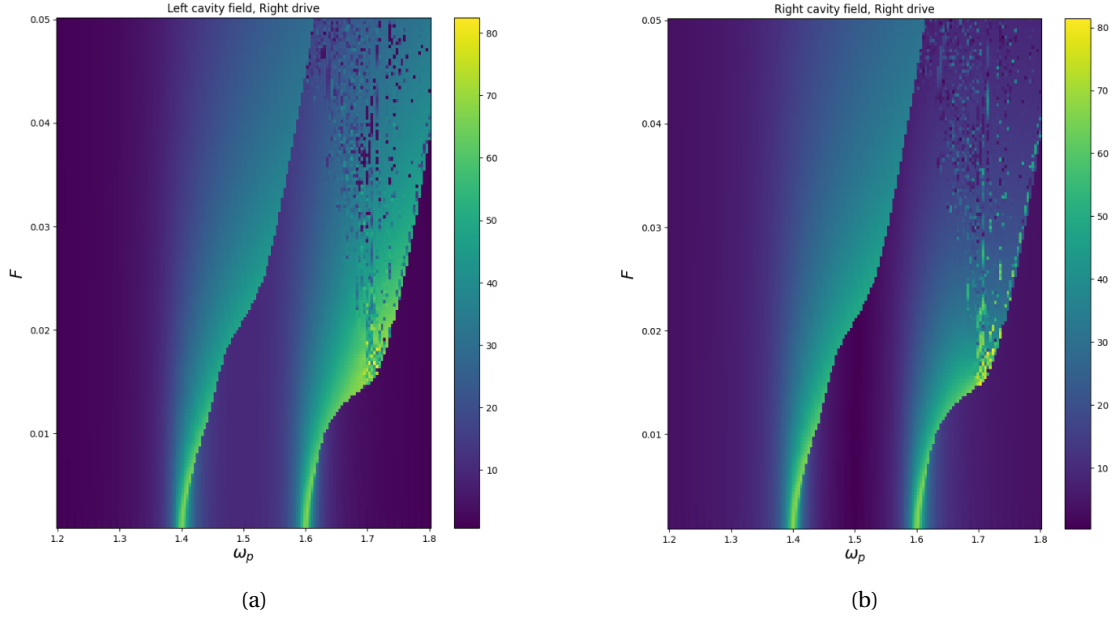


Figure 2.8: Modulus squared of the left (a) and right (b) cavity fields as a function of the pump frequency and the input power when the drive is applied on the right cavity for  $K_l = K_r$  and  $\omega_l = \omega_r$

### 2.2.2 $\omega_l > \omega_r$

We continue the analysis by setting one of the two resonant frequencies larger than the other, in this case  $\omega_r/2\pi = 1.4$  GHz and  $\omega_l/2\pi = 1.6$  GHz. The physics of the case  $\omega_r > \omega_l$  is analogous to the examined one for parallel Kerr resonators and it is not reported here. Since the detuning between the two cavities is now considerable, we can see on Fig. 2.9 that, when applying a left drive almost only the left cavity becomes populated, and viceversa when applying a right drive. This asymmetry will account for the behaviour shown on Fig. 2.10 and 2.11 in which the slope of the Kerr shift is significantly different. In such a configuration, the existence of a merging region is not assured.

## Chapter 2. Inverted and Parallel Kerr Resonators

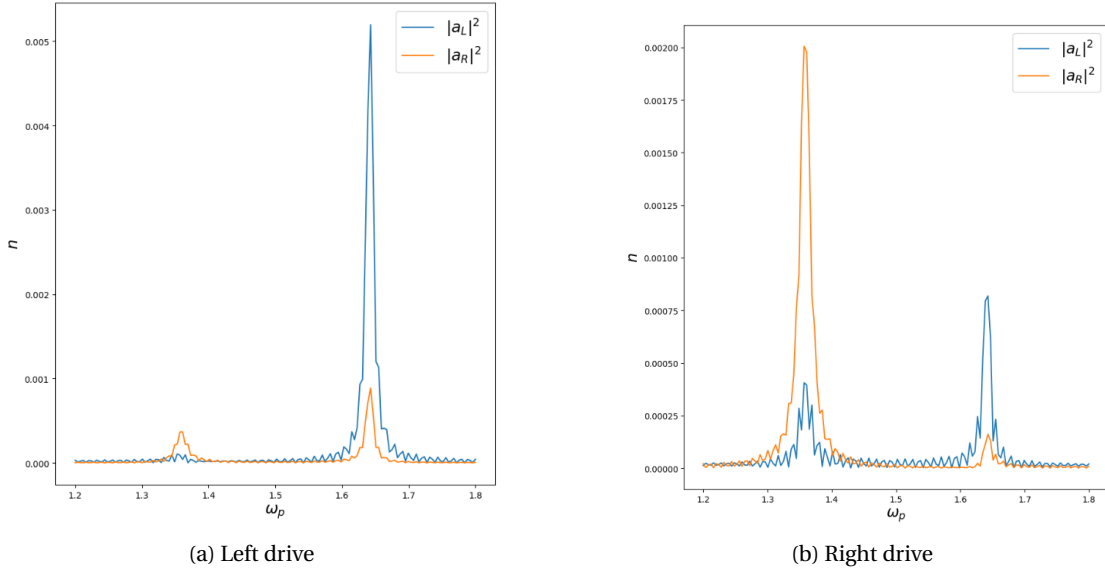


Figure 2.9: Modulus squared of the left and right cavity fields as a function of the pump frequency when the drive is applied on the left cavity (a) or on the right cavity (b) for  $K_l = K_r$  and  $\omega_l > \omega_r$

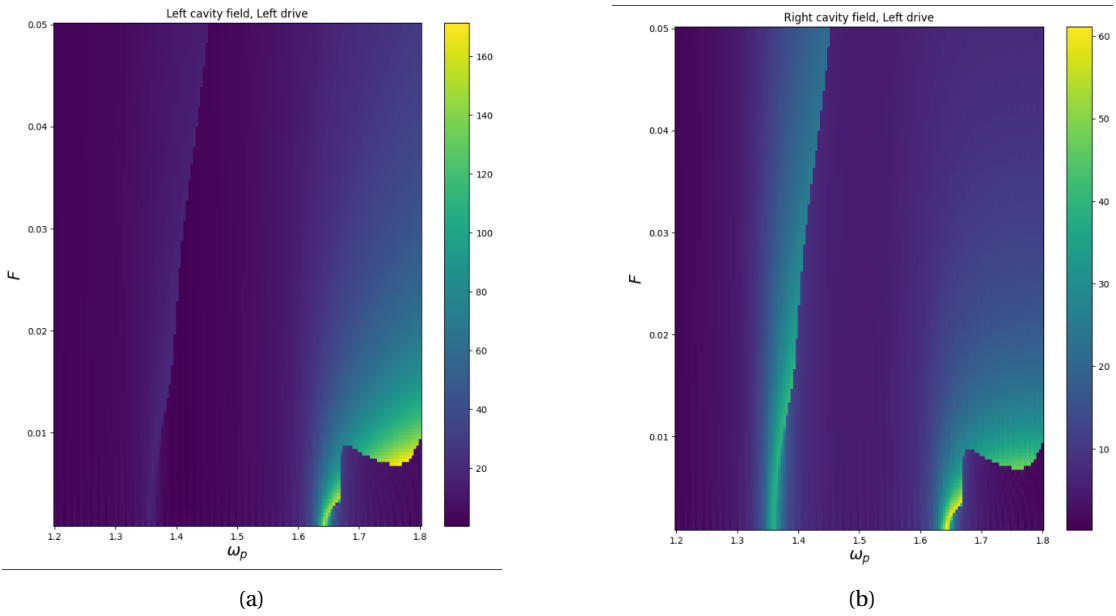


Figure 2.10: Modulus squared of the left (a) and right (b) cavity fields as a function of the pump frequency and the input power when the drive is applied on the left cavity for  $K_l = K_r$  and  $\omega_l > \omega_r$

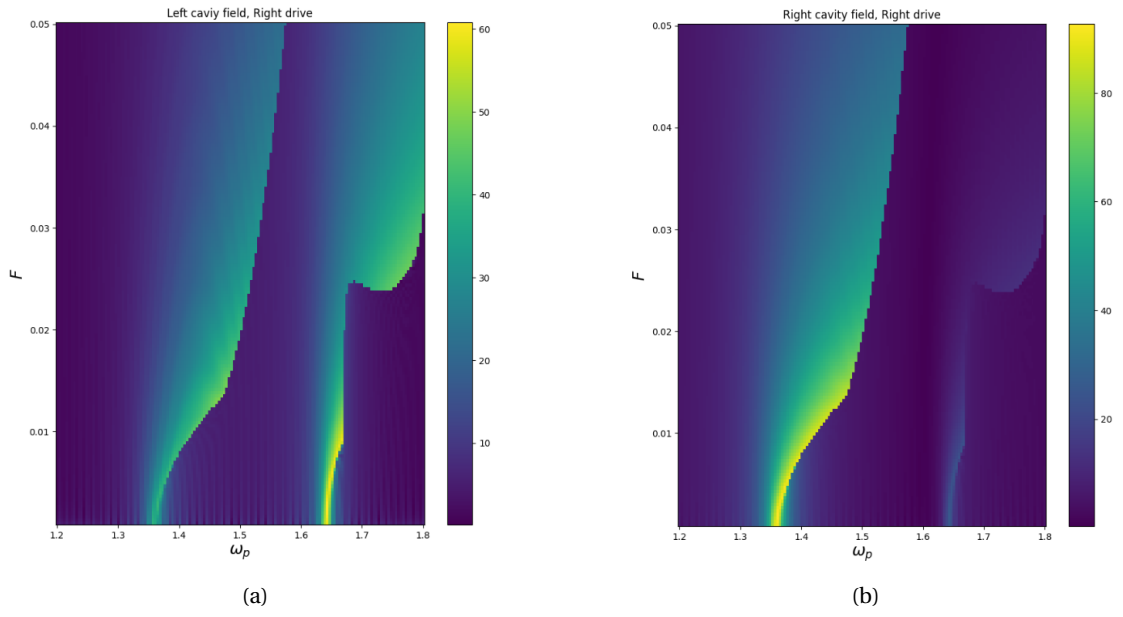


Figure 2.11: Modulus squared of the left (a) and right (b) cavity fields as a function of the pump frequency and the input power when the drive is applied on the right cavity for  $K_l = K_r$  and  $\omega_l > \omega_r$

### 2.3 Inverted Kerr

In this section we analyse the behaviour of inverted Kerr resonators; on Fig. 2.12 are represented the two configuration of interest, where dashed lines correspond to uncoupled modes and solid lines correspond to coupled modes. On Fig.2.12a the two resonator have the same resonant frequency; without coupling the two modes occupy the same initial position in frequency space and undergo a Kerr shift with the opposite slope, while with coupling they are set apart by  $2J$  and they become less and less coupled when the drive strength is increased. On Fig.2.12b the two resonator have different resonant frequency; without coupling the two modes are supposed to cross in one point in frequency space, due to their opposite Kerr term. However, when there is coupling between the resonators, the signature of an avoided crossing appear. The modes are initially uncoupled, by effect of the large detuning, then they couple in the region when the crossing is supposed to happen and, after that, they become less and less coupled when the drive strength is increased, following the path of the uncoupled case. The simulation are performed with  $K_l = K_r = 0.1$  GHz. The simulation are performed with  $K_l = -K_r = 0.1$  GHz. An intercavity coupling  $J = 100$  MHz is applied while internal coupling are set to  $\kappa = 10$  MHz and external losses are set to  $\gamma = 20$  MHz. The input drive strength is initially set at  $F = 0.5$  MHz and later varied in a range going from 0.1 MHz to 5 MHz. The equation of motion for the semi-classical fields are numerically integrated using the Runge-Kutta method of order 5.

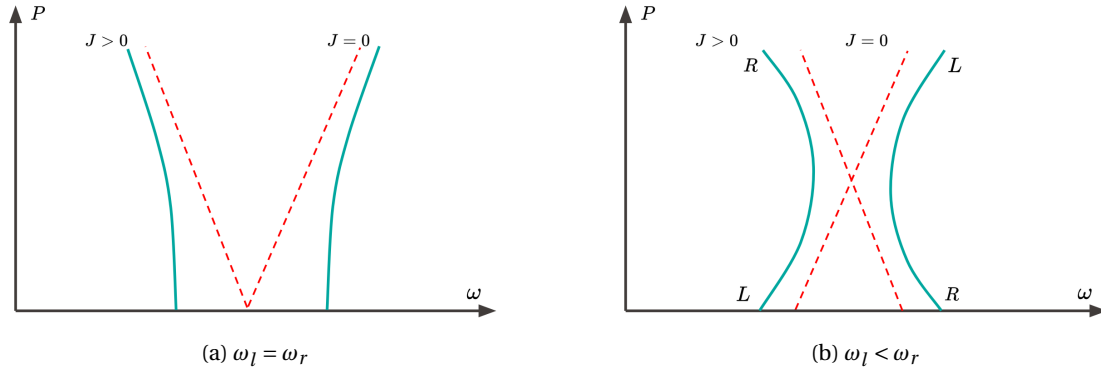


Figure 2.12: Schematic representation of the Kerr shift in an inverted Kerr dimer: dashed lines represent the uncoupled modes, solid lines represent the hybridized modes

#### 2.3.1 $\omega_l = \omega_r$

As can be appreciated on Fig. 2.13, the initial behaviour of the cavity field is analogous case for the parallel Kerr configuration. The relevant difference lies in the direction of the Kerr shift: the right cavity field is shifted to the left due to the negative Kerr, while the left cavity field is shifted to the right due to the positive Kerr, as can be seen on Fig. 2.14 and 2.15. In this setting, no merging region will arise.



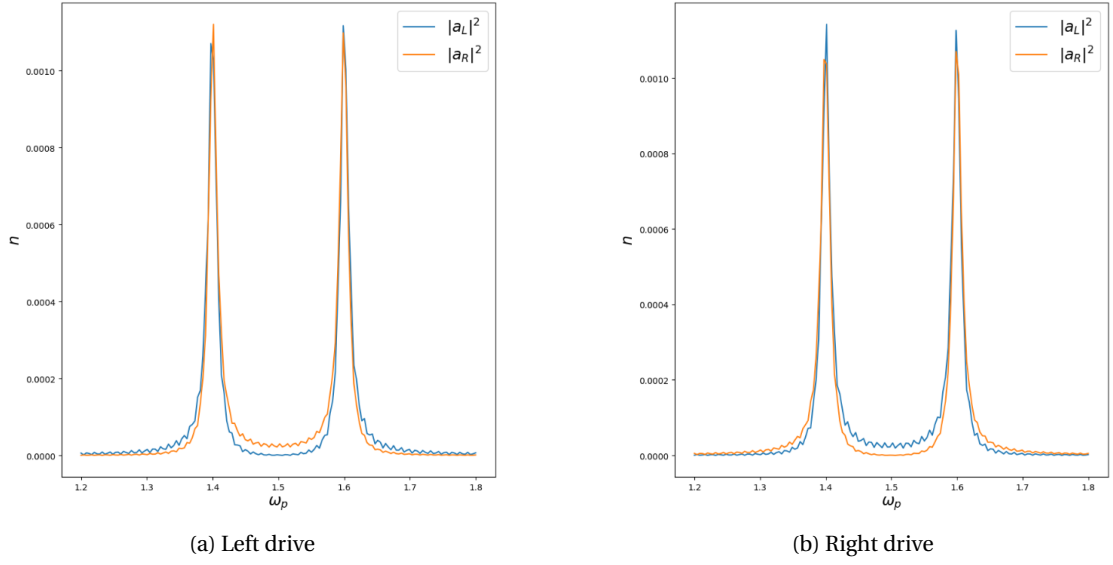


Figure 2.13: Modulus squared of the left and right cavity fields as a function of the pump frequency when the drive is applied on the left cavity (a) or on the right cavity (b) for  $K_l = -K_r$  and  $\omega_l = \omega_r$

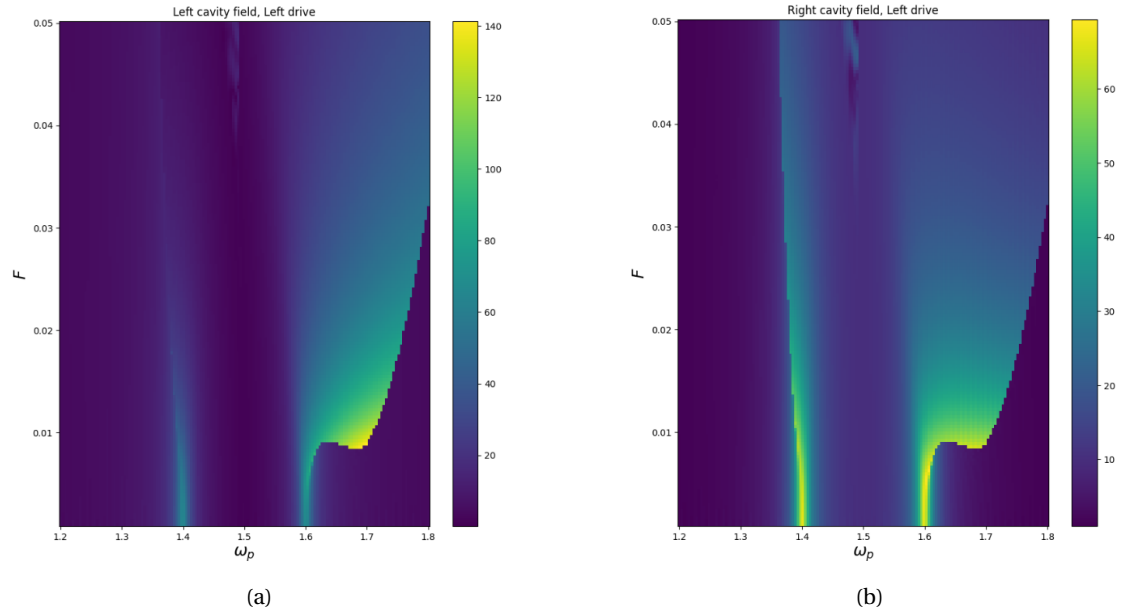


Figure 2.14: Modulus squared of the left (a) and right (b) cavity fields as a function of the pump frequency and the input power when the drive is applied on the left cavity for  $K_l = -K_r$  and  $\omega_l = \omega_r$

## Chapter 2. Inverted and Parallel Kerr Resonators

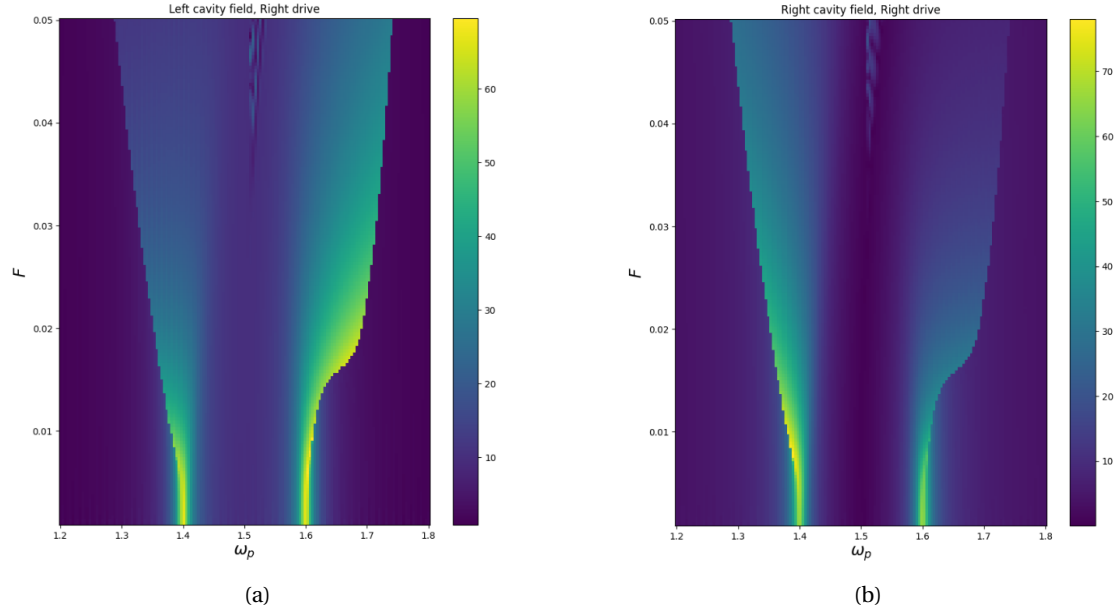


Figure 2.15: Modulus squared of the left (a) and right (b) cavity fields as a function of the pump frequency and the input power when the drive is applied on the right cavity for  $K_l = -K_r$  and  $\omega_l = \omega_r$

### 2.3.2 $\omega_l < \omega_r$

Let us analyse now the case in which  $\omega_l < \omega_r$ : since, in this case,  $\omega_r/2\pi = 1.6$  GHz and  $\omega_l/2\pi = 1.4$  GHz, and the right cavity field is shifted to the left while the left cavity field is shifted to the right, we would expect an interesting behaviour to appear in the merging region. First of all, Fig. 2.16 shows the initial cavity fields and, as discussed, the large detuning lets the modes be rather localized. On Fig. 2.17 and 2.19 is shown the cavity fields landscape as a

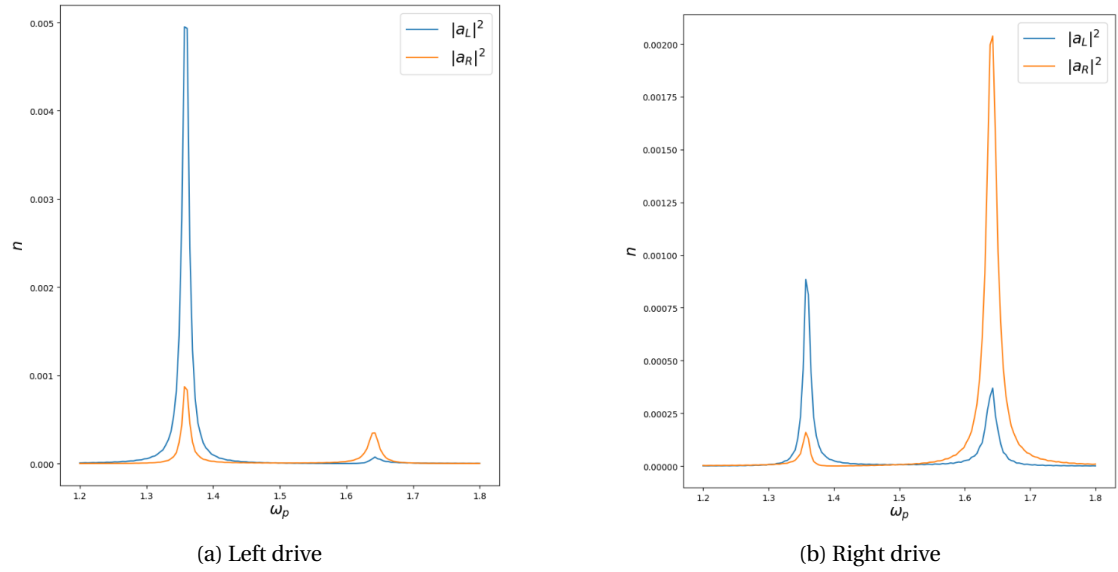


Figure 2.16: Modulus squared of the left and right cavity fields as a function of the pump frequency when the drive is applied on the left cavity (a) or on the right cavity (b) for  $K_l = -K_r$  and  $\omega_l < \omega_r$

function of the pump frequency and input drive strength. What is interesting to notice, and it is particularly apparent on Fig. 2.17b and 2.19b, is that the region in which the lines are supposed to cross is instead an empty zone. This avoided crossing is a signature of strong coupling between the cavity fields, showing the fact that the modes are fully hybridized, and it is well captured and described by the semiclassical approximation. Fig. 2.18 and 2.20 show horizontal line-cuts at approximately half of the drive strength range of the corresponding 2D plots. The interesting, and rather unseen, feature of these plots is the fact that four jumps, corresponding to as many phase transitions, can be appreciated, when two are expected in the case of a dimer. This strongly suggest a much richer phase diagram, that deserves to be analysed deeply.

## Chapter 2. Inverted and Parallel Kerr Resonators

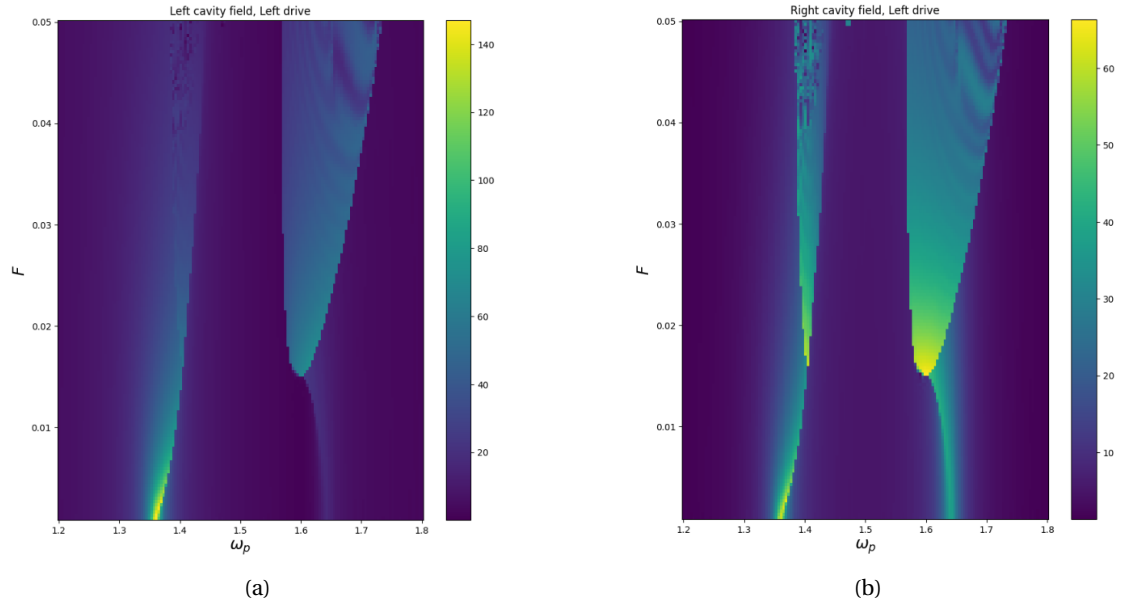


Figure 2.17: Modulus squared of the left (a) and right (b) cavity fields as a function of the pump frequency and the input power when the drive is applied on the left cavity for  $K_l = -K_r$  and  $\omega_l < \omega_r$

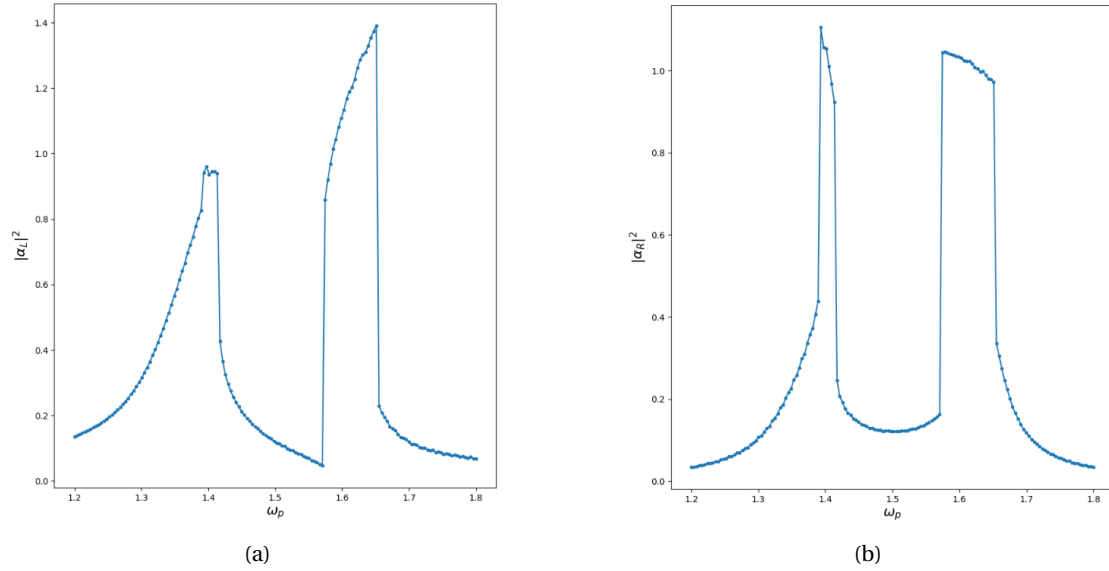


Figure 2.18: Horizontal line-cuts of the left (a) and right (b) cavity field when a drive of  $F = 2, 4$  MHz is applied on the left cavity for  $K_l = -K_r$  and  $\omega_l < \omega_r$

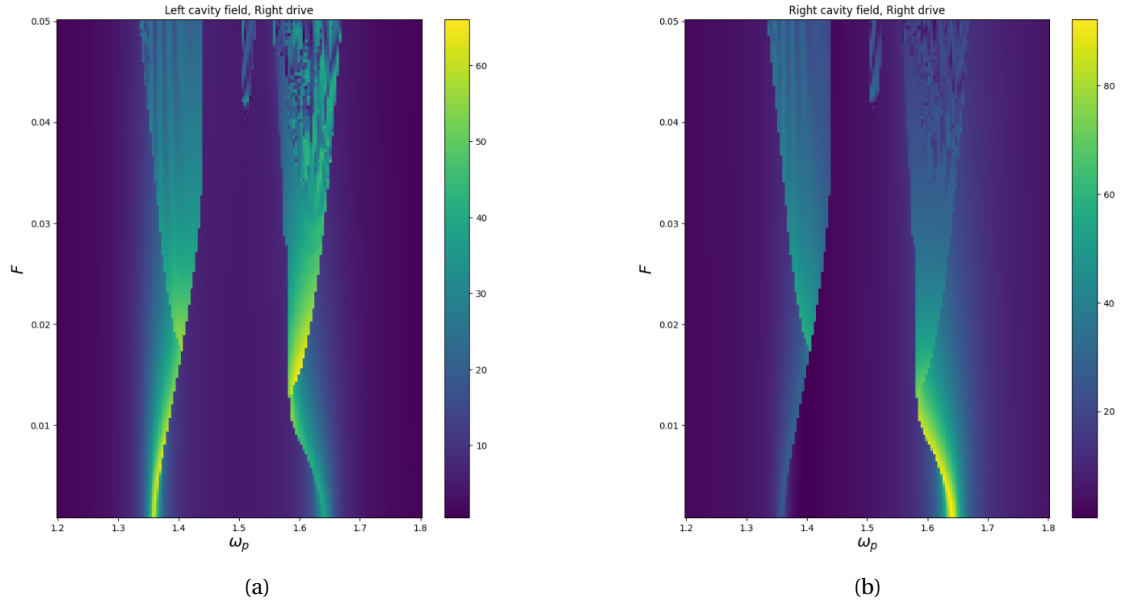


Figure 2.19: Modulus squared of the left (a) and right (b) cavity fields as a function of the pump frequency and the input power when the drive is applied on the right cavity for  $K_l = -K_r$  and  $\omega_l < \omega_r$

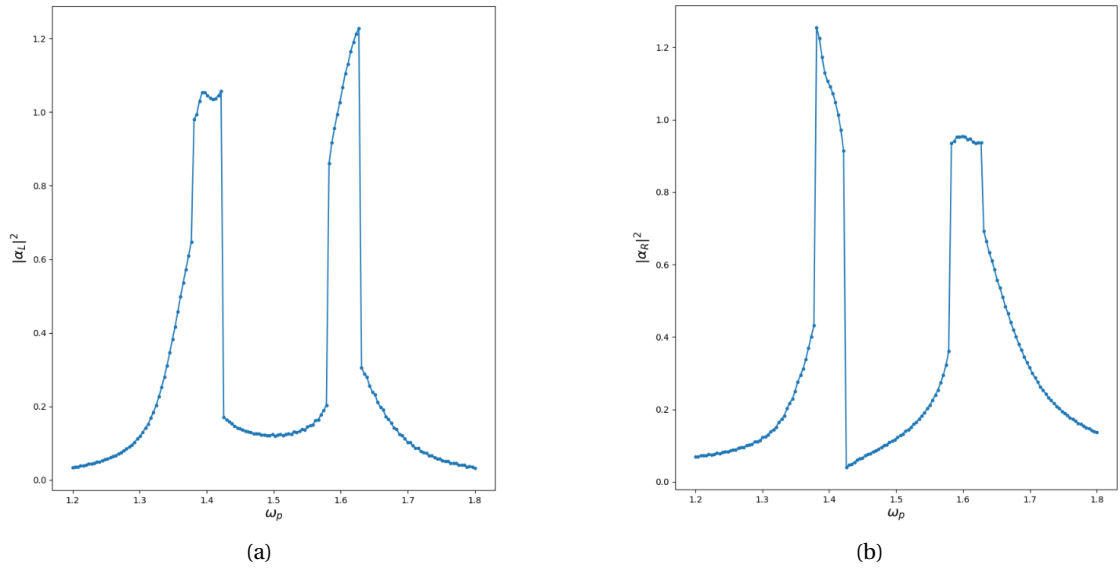


Figure 2.20: Horizontal line-cuts of the left (a) and right (b) cavity field when a drive of  $F = 2, 4$  MHz is applied on the right cavity for  $K_l = -K_r$  and  $\omega_l < \omega_r$



# **Tunable non-linearity devices**

## **Part III**





## 3 Tunable non-linearity devices

In order to experimentally produce a system that exhibits the features described in the previous part, we must engineer a device whose nonlinearity is tunable. For this reason, we start by analysing an array of SQUIDS, a device with a tunable negative Kerr non-linearity. Numerous implementations and applications of SQUID arrays can be found in the literature. Then, we analyse an array of RF-Squid, a device whose Kerr non linearity can be either positive or negative and can be fine tuned according to the needs.

### 3.1 SQUID

A useful variant of the transmon artificial atom, previously discussed, is the fluxtunable transmon, where the single Josephson junction is replaced with two parallel junctions forming a superconducting quantum interference device (SQUID), depicted on Fig. 3.1. The transmon Hamiltonian then reads:

$$\hat{H}_T = 4E_C \hat{n}^2 - E_{J1} \cos \hat{\varphi}_1 - E_{J2} \cos \hat{\varphi}_2, \quad (3.1)$$

where  $E_{Ji}$  is the Josephson energy of junction  $i$  and  $\hat{\varphi}_i$  is the phase difference across that junction. In the presence of an external flux  $\Phi_x$  threading the SQUID loop and in the limit of small geometric inductance of the loop, flux quantization requires that  $\hat{\varphi}_1 - \hat{\varphi}_2 = 2\pi\Phi_x/\Phi_0 \pmod{2\pi}$ . Defining the average phase difference as  $\hat{\varphi} = (\hat{\varphi}_1 + \hat{\varphi}_2)/2$ , the Hamiltonian can then be rewritten as:

$$\hat{H}_T = 4E_C \hat{n}^2 - E_J(\Phi_x) \cos(\hat{\varphi} - \varphi_0), \quad (3.2)$$

where

$$E_J(\Phi_x) = E_{J\Sigma} \cos\left(\frac{\pi\Phi_x}{\Phi_0}\right) \sqrt{1 + d^2 \tan^2\left(\frac{\pi\Phi_x}{\Phi_0}\right)} \quad (3.3)$$

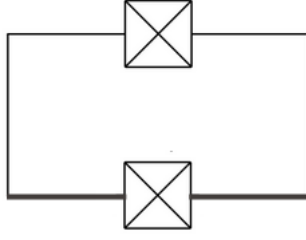


Figure 3.1: SQUID circuit diagram

with  $E_{J\Sigma} = E_{J2} + E_{J1}$  and  $d = (E_{J2} - E_{J1}) / E_{J\Sigma}$  the junction asymmetry.

The phase  $\varphi_0 = d \tan(\pi\Phi_x/\Phi_0)$  can be disregarded when dealing with a time-independent flux. Replacing the single junction with a SQUID loop then yields an effective flux-tunable Josephson energy  $E_J(\Phi_x)$ . In turn, this results in a flux-tunable transmon frequency:

$$\omega_q(\Phi_x) = \sqrt{8E_C |E_J(\Phi_x)|} - E_C / \hbar \quad (3.4)$$

As already mentioned, the SQUID has a negative non-linearity of  $-\frac{E_c}{\hbar}$ .

### 3.2 Array of SQUIDS

Fine-tuning the non-linearity of a superconducting device can be achieved by concatenating SQUIDS devices in an array fashion. The resulting circuit can be conveniently linearized and considered as an array of  $N$  LC circuits to find the analytical expression of the resonant frequency of the circuit. Then, using the compositions of inductors and capacitors, it is possible to find the equivalent inductance and the equivalent capacitance of the circuit:

$$\tilde{L} = NL_J \quad \tilde{C} = \frac{C_J}{N} * C_g \quad (3.5)$$

The resonant frequency associated with the equivalent LC circuit is:

$$\omega_{eq} = \frac{1}{\sqrt{\tilde{L}\tilde{C}}} = \frac{1}{\sqrt{NL_J \left( \frac{C_J}{N} * C_g \right)}} \quad (3.6)$$

Under some assumption the Kerr non-linearity scales as:

$$K \propto \frac{1}{N^2} \quad (3.7)$$

An array of SQUIDS will have as many modes as many are the SQUIDS composing it; however, in practice, we are most often interested in the first mode. Fig. 3.2a shows the first three modes of an array of  $N = 32$  SQUIDS with a plasma frequency of  $\omega = 39$  GHz, corresponding

to the so-called, high UV cutoff and a Josepson frequency per SQUID of  $\frac{E_J}{h} = 320$  GHz. An array of SQUIDs can only be tuned for negative value of non-linearities, which is, additionally, flux-independent, as shown on Fig. 3.2b.

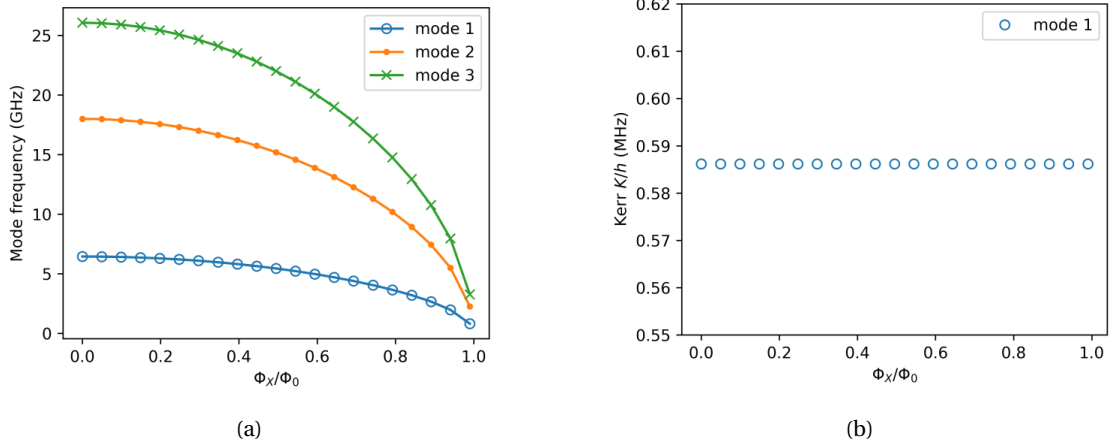


Figure 3.2: First three Eigenmodes(a) and absolute value of Kerr non-linearity (b) of an array of  $N = 32$  SQUIDs as a function of the flux.

The array of SQUIDs and the equivalent LC circuit are depicted on Fig. 3.3.

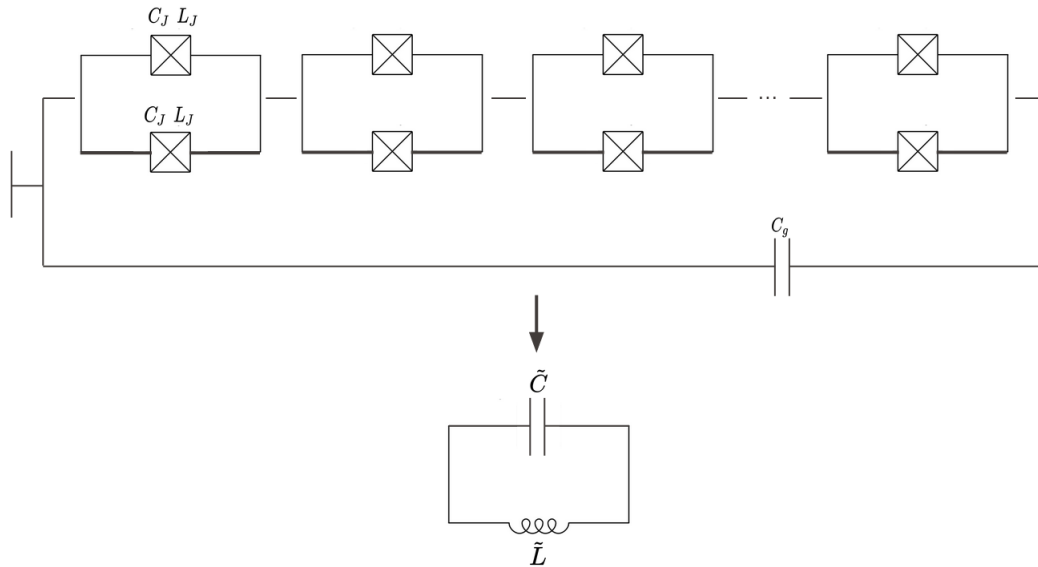


Figure 3.3: Equivalent circuit of an array of SQUIDs

### 3.3 RF-SQUID

Radio frequency superconducting quantum interference devices (RF-SQUIDS) made of conventional superconductors had been very popular some fifteen to thirty years ago. Later on, they had been replaced by dc SQUIDS, which then offered higher sensitivity. However, the operation of RF-SQUIDS at microwave bias frequencies has greatly improved their sensitivity, so that now RF-SQUIDS can be fabricated which are comparable to the best dc SQUIDS in terms of field sensitivity, as well as energy resolution. The discovery of high temperature superconductors (HTS) has further increased interest in RF-SQUIDS, mainly because the inductance of RF-SQUIDS and thus their loop area, can be made much larger than that of dc SQUIDS before a significant reduction in signal voltage is observed. Today, RF-SQUIDS are again used in numerous applications, such as biomagnetism, geophysical measurements and nondestructive evaluation.

The interesting aspect of this device is that it as a tunable non-linearity. Differently from the dc SQUID, whose non-linearity is strictly negative and flux-independent, the RF-SQUID non-linearity could be tuned to take positive and negative values. The Hamiltonian of an RF-SQUID reads:

$$\hat{H}_{RF} = 4E_C \hat{N}^2 + E_L (\hat{\phi} - \varphi_x)^2 - E_J \cos(\hat{\phi}) \quad (3.8)$$

where  $E_C, E_L, E_J$  are the charging energy, the inductive energy and the Josephson energy, respectively,  $\hat{\phi} = \phi_0 \hat{\phi}$  is the phase operator,  $\hat{N}$  is the charge operator and  $\varphi_x = \frac{\phi_x}{\phi_0}$  is the phase of the RF-SQUID. The aim is to find the explicit, flux-dependent, Kerr non-linearity of the RF-SQUID. To do so, one starts by applying the translation operator  $T = e^{i\hat{N}\varphi_x}$  to  $H_{RF}$ ; this operation corresponds to a translation in  $\varphi$ -space, such that:

$$\begin{aligned} \hat{N} &\rightarrow \hat{N} \\ \hat{\phi} &\rightarrow \hat{\phi} + \hat{\phi}_x \end{aligned} \quad (3.9)$$

The resulting Hamiltonian reads:

$$\begin{aligned} \tilde{H}_{RF} &= 4E_C \hat{N}^2 + E_L \hat{\phi}^2 - E_J \cos(\hat{\phi} + \hat{\phi}_x) \\ &= 4E_C \hat{N}^2 + E_L \hat{\phi}^2 - E_J [\cos(\hat{\phi}) \cos(\hat{\phi}_x) - \sin(\hat{\phi}) \sin(\hat{\phi}_x)] \end{aligned} \quad (3.10)$$

If the effective capacitive energy,  $E_C$ , of the mode is much smaller than the effective Josephson energy,  $E_J$ , the flux will be well localized near the bottom of the potential and thus, expanding the cosine and sine to the forth order in  $\varphi$ , one obtains:

$$\tilde{H}_{RF} \approx 4E_C \hat{N}^2 + E_L \hat{\phi}^2 + E_J \left[ \cos(\hat{\phi}_x) \left( 1 - \frac{\varphi^2}{2!} + \frac{\varphi^4}{4!} \right) - \sin(\hat{\phi}_x) \left( \varphi - \frac{\varphi^3}{3!} \right) \right] \quad (3.11)$$

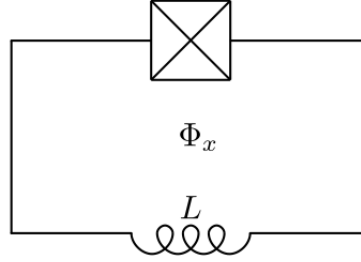


Figure 3.4: RF-SQUID circuit diagram

Exploiting Eqs. 1.10 and 1.12, one obtains the second-quantized Hamiltonian:

$$\begin{aligned} \hat{H}_{RF} = & -\frac{2E_C}{\zeta}(\hat{c} - \hat{c}^\dagger)^2 + \frac{E_L\zeta}{2}(\hat{c} + \hat{c}^\dagger)^2 \\ & - E_J[\cos(\hat{\varphi}_x) \left[ 1 - \frac{\zeta}{4}(\hat{c} + \hat{c}^\dagger)^2 + \frac{\zeta^2}{96}(\hat{c} + \hat{c}^\dagger)^4 \right] \\ & - \sin(\hat{\varphi}_x) \left[ \sqrt{\frac{\zeta}{2}}(\hat{c} + \hat{c}^\dagger) - \frac{\zeta}{2}\sqrt{\frac{\zeta}{2}}(\hat{c} + \hat{c}^\dagger)^3 \right]] \end{aligned} \quad (3.12)$$

Using the commutation relation and the easily verified relations,

$$\begin{aligned} [c, (c^\dagger)^k] &= k(c^\dagger)^{k-1} \\ [c^\dagger, c^k] &= -kc^{k-1} \end{aligned} \quad (3.13)$$

expanding powers and applying the rotating wave approximation in order to keep only excitations preserving terms, one obtains the following normal-ordered Hamiltonian:

$$\hat{H}_{RF} = \left( \frac{4E_C}{\zeta} + E_L\zeta + \frac{E_J\zeta}{2}\cos(\varphi_x) - \frac{E_J\zeta^2}{8}\cos(\varphi_x) \right) c^\dagger c - \frac{E_J\zeta^2}{16}\cos(\varphi_x)(c^\dagger)^2 c^2 \quad (3.14)$$

Or, expliciting the definition of  $\zeta$ :

$$\begin{aligned} \hat{H}_{RF} = & (4\sqrt{E_C(E_L + E_J/2)} + \sqrt{\frac{E_L^2(E_L + E_J/2)}{4E_C}} + \frac{1}{4}\sqrt{\frac{E_J(E_L + E_J/2)}{E_C}}\cos(\varphi_x) \\ & - \frac{1}{32}\frac{E_J(E_L + E_J/2)}{E_C}\cos(\varphi_x))c^\dagger c - \frac{1}{64}\frac{E_J(E_L + E_J/2)}{E_C}\cos(\varphi_x)(c^\dagger)^2 c^2 \end{aligned} \quad (3.15)$$

where

$$\begin{aligned} \omega_{RF} = & \frac{1}{\hbar}(4\sqrt{E_C(E_L + E_J/2)} + \sqrt{\frac{E_L^2(E_L + E_J/2)}{4E_C}} + \frac{1}{4}\sqrt{\frac{E_J(E_L + E_J/2)}{E_C}}\cos(\varphi_x) \\ & - \frac{1}{32}\frac{E_J(E_L + E_J/2)}{E_C}\cos(\varphi_x)) \end{aligned} \quad (3.16)$$

### Chapter 3. Tunable non-linearity devices

$$K_{RF} = -\frac{1}{\hbar} \frac{1}{64} \frac{E_J(E_L + E_J/2)}{E_C} \cos(\varphi_x) \quad (3.17)$$

are the resonant frequency and Kerr non-linearity of the RF-SQUID, respectively. As expected, the Kerr non-linearity explicitly depends on the flux inside the RF-SQUID.

#### 3.3.1 Numeric simulations

To better understand the physics of the RF-SQUIDS and the validity of the analytical results, several simulations were carried out using the python library scQubits. On Fig. 3.5a are plotted the energy levels shifted by the ground state energy of an RF-SQUID with  $\frac{E_J}{\hbar} = 100$  GHz,  $\frac{E_L}{\hbar} = 500$  GHz,  $\frac{E_C}{\hbar} = 0.5$  GHz against flux; the plot shows that for such parameters the resonant frequency of the RF-SQUID is approximately 50 GHz, which corresponds to the first transition. Fig. 3.5b shows the anharmonicity of the RF-SQUID as a function of the flux; as mentioned, it oscillates to take both positive and negative values.

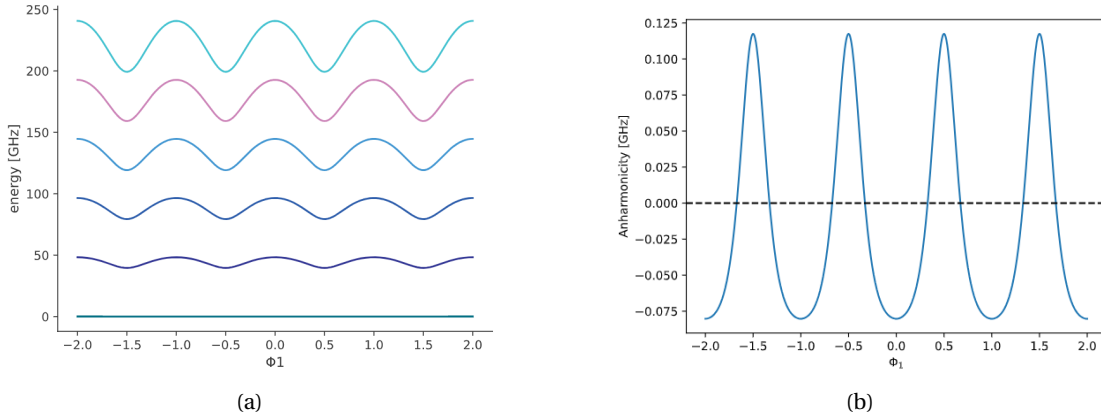


Figure 3.5: Energy levels relative to the ground state energy (a) and anharmonicity (b) of an RF-SQUID with  $\frac{E_J}{\hbar} = 100$  GHz,  $\frac{E_L}{\hbar} = 500$  GHz,  $\frac{E_C}{\hbar} = 0.5$  GHz

The simulations are carried out using the harmonic basis for the Hamiltonian and taking as relevant variable the flux inside the RF-SQUID. The default dimension of the Hilbert space in scQubits for a single RF-SQUID is 30, which means that the total dimension of the Hilbert space for an array of  $N$  RF-SQUID will scale as  $30^N$ . This is a huge number and a terrible scaling, and it is not necessary to use such a large Hilbert space to get accurate results. The cutoff parameter allows to reduce the dimension of the Hilbert space by truncating the number of states in the harmonic basis. The cutoff parameter can be set individually for each RF-SQUID in the array. Fig. 3.6 and 3.7 shows the precision on ground state energy as a function of the cutoff, changing  $E_J$  and keeping  $E_L$  constant or changing  $E_L$  and keeping  $E_J$  constant, respectively. To obtain a faster convergence we set the ratio  $E_L/E_J = 50$ , while keeping  $E_L/E_C \gg 1$  and  $E_J/E_C \gg 1$ .

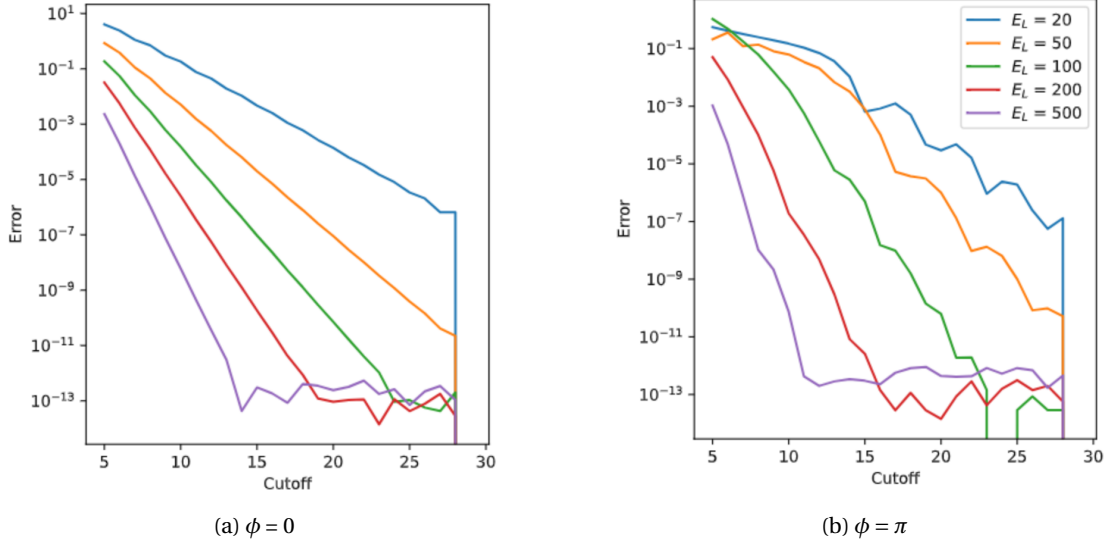


Figure 3.6: Precision on the energy as a function of the cutoff on the flux variable for different values of  $E_J$  while keeping  $E_L = 500h$  GHz.

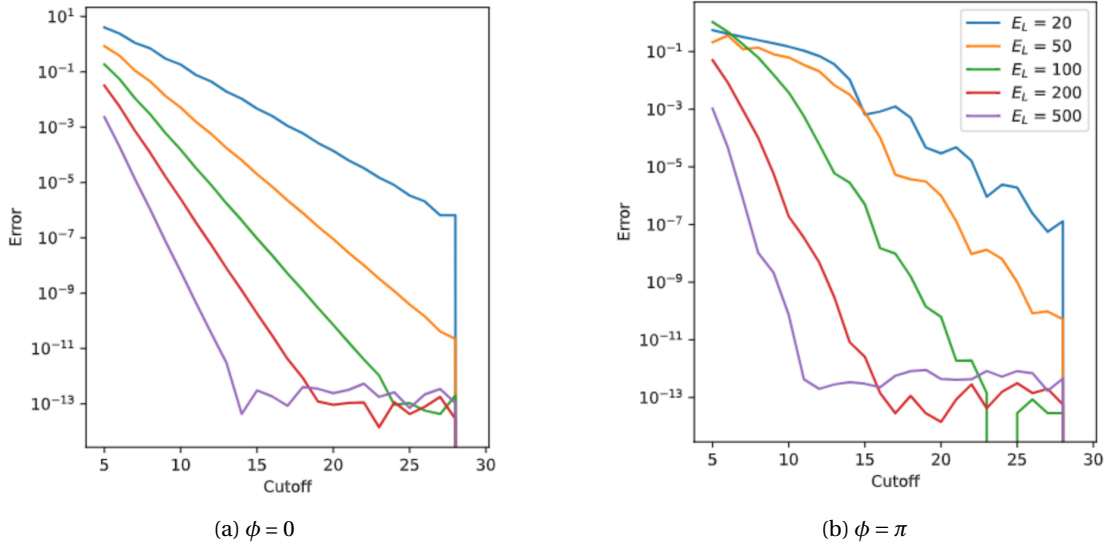


Figure 3.7: Precision on the energy as a function of the cutoff on the flux variable for different values of  $E_L$  while keeping  $E_J = 100h$  GHz.

### 3.4 Array of RF-SQUIDs

As for the array of SQUIDs, we want to target specific values of resonant frequency and Kerr-nonlinearity that are experimentally realizable. In particular, one should design a device with a resonant frequency of about 5 GHz and a non linearity of about 1 MHz; such a value of non-linearity is of particular interest since it corresponds to the typical dissipation rate of the system and one could analyse the classical-to-quantum transitions, in which the system is alternately dominated by dissipations or non-linearity. The array of RF-SQUIDs that is examined here is composed of  $N$  identical RF-SQUIDs, with Josephson inductance  $L_J$ , Josephson capacitance  $C_J$ , and geometrical inductance  $L$ . A geometric capacitance  $C_g$  is set in parallel with the array.

#### 3.4.1 Equivalent circuit

In order to find the analytical expression of the resonant frequency of an array of RF-SQUIDs, it is convenient to linearize the circuit and consider it as an array of  $N$  LC circuits. Then, using the compositions of inductors and capacitors, it is possible to find the equivalent inductance and the equivalent capacitance of the circuit:

$$\tilde{L} = N \frac{L_J L}{L_J + L} \quad \tilde{C} = \frac{C_J}{N} * C_g \quad (3.18)$$

The resonant frequency associated with the equivalent LC circuit is:

$$\omega_{eq} = \frac{1}{\sqrt{\tilde{L}\tilde{C}}} = \frac{1}{\sqrt{N \frac{L_J L}{L_J + L} \left( \frac{C_J}{N} * C_g \right)}} \quad (3.19)$$

In analogy with the array of SQUIDs, we make the assumption, to be verified experimentally, that the Kerr non-linearity scales as:

$$K \propto \frac{1}{N^2} \quad (3.20)$$

The array of RF-SQUIDs and the equivalent LC circuit are depicted on Fig. 3.8. Numerically verifying Eqs. (3.19) and (3.20) is computationally demanding for the bad scaling of the Hilbert space as a function of the number of RF-SQUIDs in the array. This limiting factor is apparent on Fig. 3.9 and 3.9: the precision reached in the case  $N=5$  was of the order of 10 for a cutoff of 8, which lead to unphysical results. More advanced techniques could be used to overcome such a limitation and could be the topic of further developpements of this project.



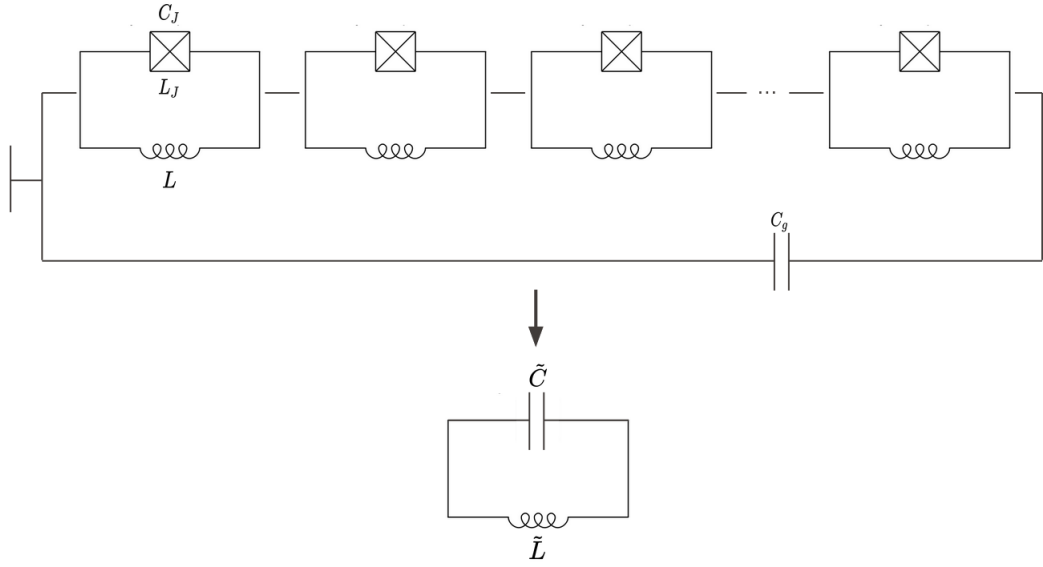


Figure 3.8: Equivalent circuit of an array of RF-SQUIDs

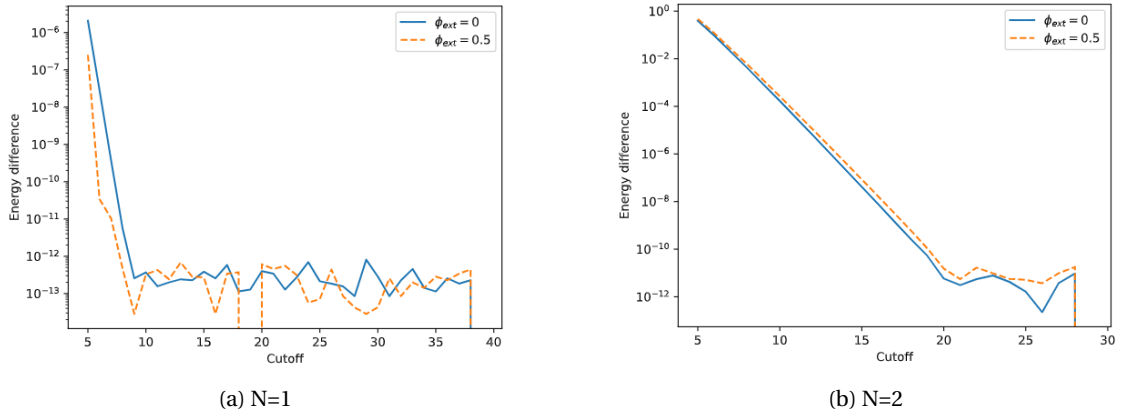


Figure 3.9: Precision on the energy as a function of the cutoff on the flux variable for  $E_J = 50h$ , GHz  $E_L = 2500h$  GHz and  $E_C = 0.5h$  GHz.

### Chapter 3. Tunable non-linearity devices

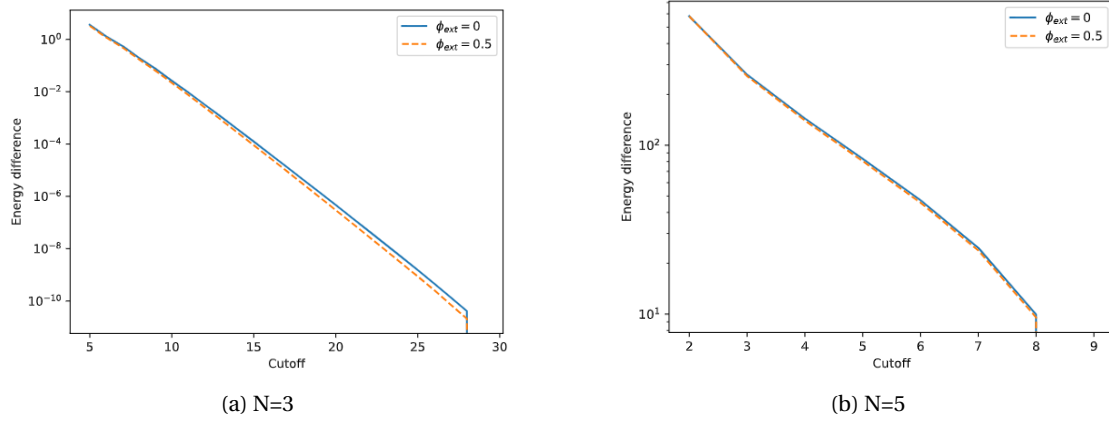


Figure 3.10: Precision on the energy as a function of the cutoff on the flux variable for  $E_J = 50h$ , GHz  $E_L = 2500h$  GHz and  $E_C = 0.5h$  GHz.

# **Experimental Design** **Part IV**



# Bibliography

- Antonio Rubio Abadal. Josephson Parametric Amplifiers with Lumped-element Coupled Resonators. *Master thesis*, 2015.
- Sai Pavan Chitta, Tianpu Zhao, Ziwen Huang, Ian Mondragon-Shem, and Jens Koch. Computer-aided quantization and numerical analysis of superconducting circuits. *New Journal of Physics*, 24(10):103020, October 2022. ISSN 1367-2630. doi: 10.1088/1367-2630/ac94f2. URL <https://iopscience.iop.org/article/10.1088/1367-2630/ac94f2>.
- Olesia Dmytruk, R. H. Rodriguez, Ç Ö Girit, and Marco Schiró. Theory of high-power excitation spectra of rf-SQUID. *Physical Review B*, 104(21):214508, December 2021. ISSN 2469-9950, 2469-9969. doi: 10.1103/PhysRevB.104.214508. URL <http://arxiv.org/abs/2107.07971>. arXiv:2107.07971 [cond-mat].
- C. Eichler, Y. Salathe, J. Mlynek, S. Schmidt, and A. Wallraff. Quantum limited amplification and entanglement in coupled nonlinear resonators. *Physical Review Letters*, 113(11):110502, September 2014. ISSN 0031-9007, 1079-7114. doi: 10.1103/PhysRevLett.113.110502. URL <http://arxiv.org/abs/1404.4643>. arXiv:1404.4643 [quant-ph].
- J. Griesmar, R. H. Rodriguez, V. Benzoni, J.-D. Pillet, J.-L. Smir, F. Lafont, and Ç. Ö. Girit. Superconducting on-chip spectrometer for mesoscopic quantum systems. *Physical Review Research*, 3(4):043078, October 2021. doi: 10.1103/PhysRevResearch.3.043078. URL <https://link.aps.org/doi/10.1103/PhysRevResearch.3.043078>. Publisher: American Physical Society.
- Peter Groszkowski and Jens Koch. Scqubits: a Python package for superconducting qubits. *Quantum*, 5:583, November 2021. doi: 10.22331/q-2021-11-17-583. URL <https://quantum-journal.org/papers/q-2021-11-17-583/>. Publisher: Verein zur Förderung des Open Access Publizierens in den Quantenwissenschaften.
- M. Khabipov, V. Gaydamachenko, C. Kissling, R. Dolata, and A. B. Zorin. Superconducting microwave resonators with non-centrosymmetric nonlinearity. *Superconductor Science and Technology*, 35(6):065020, June 2022. ISSN 0953-2048, 1361-6668. doi: 10.1088/1361-6668/ac6989. URL <http://arxiv.org/abs/2204.10133>. arXiv:2204.10133 [cond-mat].
- Vlad E. Manucharyan, Jens Koch, Leonid I. Glazman, and Michel H. Devoret. Fluxonium: Single Cooper-Pair Circuit Free of Charge Offsets | Science, 2009. URL <https://www.science.org/doi/full/10.1126/science.1175552>.

## Bibliography

---

- Ofer Naaman and José Aumentado. Synthesis of Parametrically Coupled Networks. *PRX Quantum*, 3(2):020201, May 2022. ISSN 2691-3399. doi: 10.1103/PRXQuantum.3.020201. URL <https://link.aps.org/doi/10.1103/PRXQuantum.3.020201>.
- A. Opremcak, I. Pechenezhskiy, C. Howington, B. Christensen, Matthew Beck, Edward Leonard Jr, J. Suttle, C. Wilen, Konstantin Nesterov, G. Ribeill, Travis Thorbeck, F. Schlenker, Maxim Vavilov, B. Plourde, and R. McDermott. Measurement of a Superconducting Qubit with a Microwave Photon Counter. *Science*, 361, March 2018. doi: 10.1126/science.aat4625.
- Matilda Peruzzo, Farid Hassani, Gregory Szep, Andrea Trioni, Elena Redchenko, Martin Žemlička, and Johannes M. Fink. Geometric Superinductance Qubits: Controlling Phase Delocalization across a Single Josephson Junction. *PRX Quantum*, 2(4):040341, November 2021. ISSN 2691-3399. doi: 10.1103/PRXQuantum.2.040341. URL <https://link.aps.org/doi/10.1103/PRXQuantum.2.040341>.
- S.E. Rasmussen, K.S. Christensen, S.P. Pedersen, L.B. Kristensen, T. Bækkegaard, N.J.S. Loft, and N.T. Zinner. Superconducting Circuit Companion—an Introduction with Worked Examples. *PRX Quantum*, 2(4):040204, December 2021. ISSN 2691-3399. doi: 10.1103/PRXQuantum.2.040204. URL <https://link.aps.org/doi/10.1103/PRXQuantum.2.040204>.
- Marco Scigliuzzo, Giuseppe Calajò, Francesco Ciccarello, Daniel Perez Lozano, Andreas Bengtsson, Pasquale Scarlino, Andreas Wallraff, Darrick Chang, Per Delsing, and Simone Gasparinetti. Controlling Atom-Photon Bound States in an Array of Josephson-Junction Resonators. *Physical Review X*, 12(3):031036, September 2022. ISSN 2160-3308. doi: 10.1103/PhysRevX.12.031036. URL <https://link.aps.org/doi/10.1103/PhysRevX.12.031036>.
- Uri Vool and Michel H. Devoret. Introduction to Quantum Electromagnetic Circuits. *International Journal of Circuit Theory and Applications*, 45(7):897–934, July 2017. ISSN 0098-9886, 1097-007X. doi: 10.1002/cta.2359. URL <http://arxiv.org/abs/1610.03438>. arXiv:1610.03438 [cond-mat, physics:quant-ph].
- T. Weißl, B. Küng, E. Dumur, A. K. Feofanov, I. Matei, C. Naud, O. Buisson, F. W. J. Hekking, and W. Guichard. Kerr coefficients of plasma resonances in Josephson junction chains. *Physical Review B*, 92(10):104508, September 2015. doi: 10.1103/PhysRevB.92.104508. URL <https://link.aps.org/doi/10.1103/PhysRevB.92.104508>. Publisher: American Physical Society.